Available online at www.sciencedirect.com
SCIENCE DIRECT®
Icarus 176 (2005) 155–174
ICARUS
www.elsevier.com/locate/icarus

Saturn's cloud structure and temporal evolution from ten years of Hubble Space Telescope images (1994–2003)

S. Pérez-Hoyos [a,*], A. Sánchez-Lavega [a], R.G. French [b], J.F. Rojas [c]

[a] *Departamento de Física Aplicada I, E.T.S. Ingenieros, Universidad del País Vasco, Alameda de Urquijo s/n, 48013 Bilbao, Spain*
[b] *Department of Astronomy, Wellesley College, Wellesley, MA 02481, USA*
[c] *Departamento de Física Aplicada I, E.U.I.T.I., Universidad del País Vasco, Plaza Casilla s/n, 48013 Bilbao, Spain*

Received 26 March 2004; revised 15 January 2005

Available online 24 March 2005

Abstract

We present a study of the vertical structure of clouds and hazes in the upper atmosphere of Saturn's Southern Hemisphere during 1994–2003, about one third of a Saturn year, based on Hubble Space Telescope images. The photometrically calibrated WFPC2 images cover the spectral region between the near-UV (218–255 nm) and the near-IR (953–1042 nm), including the 890 nm methane band. Using a radiative transfer code, we have reproduced the observed center-to-limb variations in absolute reflectivity at selected latitudes which allowed us to characterize the vertical structure of the entire hemisphere during this period. A model atmosphere with two haze layers has been used to study the variation of hazes with latitude and to characterize their temporal changes. Both hazes are located above a thick cloud, putatively composed of ammonia ice. An upper thin haze in the stratosphere (between 1 and 10 mbar) is found to be persistent and formed by small particles (radii ∼0.2 μm). The lower thicker haze close to the tropopause level shows a strong latitudinal dependence in its optical thickness (typically $\tau \sim 20$–40 at the equator but $\tau \sim 5$ at the pole, at 814 nm). This tropospheric haze is blue-absorbent and extends from 50 to 100 mbar to about ∼400 mbar. Both hazes show temporal variability, but at different time-scales. First, there is a tendency for the optical thickness of the stratospheric haze to increase at all latitudes as insolation increases. Second, the tropospheric haze shows mid-term changes (over time scales from months to 1–2 years) in its optical thickness (typically by a factor of 2). Such changes always occur within a rather narrow latitude band (width ∼5–10°), affecting almost all latitudes but at different times. Third, we detected a long-term (∼10 year) decrease in the blue single-scattering albedo of the tropospheric haze particles, most intense in the equatorial and polar areas. Long-term changes follow seasonal insolation variations smoothly without any apparent delay, suggesting photochemical processes that affect the particles optical properties as well as their size. In contrast, mid-term changes are sudden and show various time-scales, pointing to a dynamical origin.

Keywords: Atmospheres, structure; Atmospheres, evolution; Saturn, atmosphere; Radiative transfer

1. Introduction

The determination of the physical and optical properties of cloud and haze particles in the stratospheres and upper tropospheres of the giant planets is essential for a host of atmospheric investigations. For example, for dynamical studies, the ranges of heights of cloud features tracked to measure the winds are key observations about the general circulation of both Jupiter and Saturn. The Galileo probe descent into Jupiter (Young, 2003) and, more recently, the discovery of a truncation in the intense Equatorial jet of Saturn (Sánchez-Lavega et al., 2003) have addressed the question of the possible height and time dependence of the winds below the upper cloud level. However, the clouds and hazes are not simply passive objects, but they also force atmospheric motions. This is accomplished by heating and cooling the atmosphere at different levels, through the absorption or reflection of both sunlight and the thermal emission coming from the deep interior. The way in which an

* Corresponding author. Fax: +34-94-601-41-78.
E-mail address: wubpehos@bi.ehu.es (S. Pérez-Hoyos).

0019-1035/$ – see front matter
doi:10.1016/j.icarus.2005.01.014

Table 1
Saturn's upper clouds and hazes studies

Reference	Observation	Epoch	Number of layers	Latitude range	Spectral coverage (μm)
Macy, 1977	Ground-based	∼1970	3	EZ–STZ	0.3–1.1
West et al., 1983	Voyager 2	1981	1–2	NH	0.264/0.75
Tomasko and Doose, 1984	Pioneer 11	1979	2	25° S–55° N	0.44/0.64
Karkoschka and Tomasko, 1992	Ground-based	1986–1989	2	NH	0.46–0.94
Karkoschka and Tomasko, 1993	HST	1991	2	NH	0.3–0.89
Ortiz et al., 1996	Ground-based	1991–1993	3	NH	0.6–0.96
Acarreta and Sánchez-Lavega, 1999	Ground-based	1990	2	EZ–NEB	0.336–0.89
Stam et al., 2001	Ground-based	1995	3	NH/SH	1.45–2.5
Muñoz et al., 2004	HST	1997	3	NH/SH	0.23–0.89
This work	HST	1994–2003	3	SH	0.255–1.042

Note. EZ—Equatorial Zone; STZ—South Temperate Zone; NEB—North Equatorial Belt; NH—Northern Hemisphere; SH—Southern Hemisphere.

atmosphere reacts to such processes is still uncertain even for our planet (see, for example, Ramanathan et al., 2001). It has long been known that Saturn has a thick haze layer close to the tropopause (Tomasko et al., 1984). In general, it has been interpreted as the result of overshooting convection from the ammonia cloud expected to exist at ∼1.4 bar based on thermochemical modelling (Weidenschilling and Lewis, 1973) and radio observations (Briggs and Sackett, 1989; Grossman et al., 1989). However, the optical properties of the particles forming such a haze (Karkoschka and Tomasko, 1993) are not at all similar to those of fresh ammonia ice (Martonchik et al., 1984), so a chromophore species is expected to be interacting with ammonia at these levels (Macy, 1977). Well above the tropospheric haze, an additional optically thin haze layer seems to be present as well (Tomasko et al., 1984, and references therein). These small particles of uncertain origin (Karkoschka and Tomasko, 1993) are particularly important at polar latitudes, where they produce an intense absorption at near-UV wavelengths. Deeper in the atmosphere, below the 1.4 bar level, many different clouds are supposed to form (Weidenschilling and Lewis, 1973) but they are well below the level that can be sounded from remote observations using optical telescopes.

This kind of three-layers model have proved to be very useful to analyze a variety of observations. Ortiz et al. (1996) successfully studied ground-based observations of Saturn in the period after the 1990 Great White Storm. Stam et al. (2001) obtained a similar model atmosphere from observations in the H (1.45–1.8 μm) and K-band (1.95–2.5 μm) in the ring-crossing epoch. More recently, Muñoz et al. (2004) interestingly compared model results from northern and southern latitudes in 1997 to retrieve information about seasonal changes in Saturn's atmosphere. These works are summarized in Table 1, where we show the reference, the kind and epoch of observations, the number of layers assumed in the model atmosphere, the latitude range and the spectral coverage.

Historical observations provide relatively good coverage of the time-dependence of Saturn's cloud stratigraphy from photometric studies at visual wavelengths starting in the 1970's (see Table 1). Unfortunately, the cross-calibration problems that arise when using different instruments and

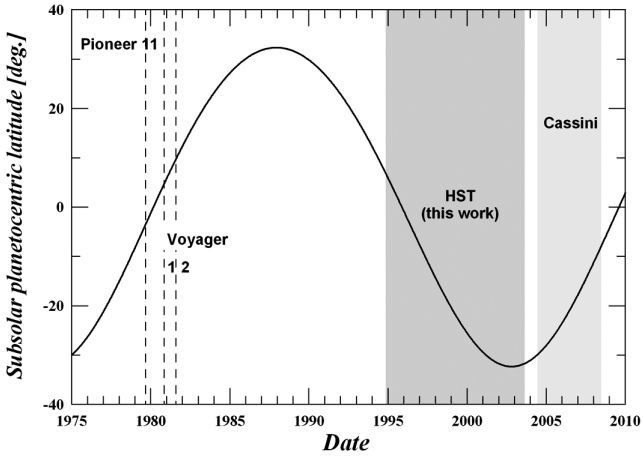

Fig. 1. The seasonal cycle of Saturn is shown as the variation of the sub-solar planetocentric latitude with time. The maximum of the sub-solar latitude is the Northern Hemisphere summer solstice (southern winter solstice) and vice versa. The equinoxes take place when the sub-solar latitude is zero. We also show the visits of the Pioneer 11, Voyager 1, and Voyager 2 with dashed lines and, as shaded areas, our period of study and the expected Cassini time period.

numerical models make it quite difficult to compare many of these studies. Seasonal reflectivity variations also affect model comparisons. At the ring plane crossing epoch, the hemisphere emerging from summer is brighter at short (and darker at long) wavelengths than the winter hemisphere. This has usually been attributed to a hazier atmosphere in the cold region (West, 1982, or Sánchez-Lavega et al., 1993, and references therein).

In this paper, we investigate the stratigraphy of the upper clouds using a homogeneous set of high quality Hubble Space Telescope (HST) imaging observations obtained with WFPC2 (from UV to near-IR) spanning a decade (a third of a Saturn year), long enough to reveal both seasonal and dynamical variability. Here, we analyze the center-to-limb variation of the absolute reflectivity at selected latitudes from the near-UV (255 nm) to the near-IR (1042 nm). Our long-term study complements the period that will be covered by the Cassini mission (see Fig. 1). The spatial resolution obtained with HST images is outstanding, and allows a detailed

description of latitudinal variations and even of individual features (Sánchez-Lavega et al., 2004).

Given that the most recent ring plane crossing epoch was in 1995, our work covers the beginning of the southern summer, until after summer solstice, just as the Voyager observations covered Saturn's Northern Hemisphere, one half of an orbital period earlier. A key difference between both situations is that in 1990 (Sánchez-Lavega et al., 1991) and 1994 (Sánchez-Lavega et al., 1996) a Great White Storm and a secondary phenomenon perturbed the Equatorial Region. Apart from characterizing the upper hazes, we would like to know whether the long-term changes known to occur in Saturn's atmosphere are gradual or abrupt, as well as how the perturbation induced in the atmosphere by the storms propagated, if it did. In contrast to the Equatorial Zone, the Southern Polar Region changes seasonally from no insolation at all to continuous illumination. Studying this region could tell us a great deal about the role of sunlight in producing variations in cloud structure. This issue is important to determining the relative influence of thermal emission from the deep interior, and variable solar illumination, on Saturn's atmospheric dynamics.

In the next section, we discuss the observations, image reduction, photometric calibration and other aspects of the data set. In Section 3, we present the basics of our model atmosphere, its underlying assumptions, and the basic structure used to fit data, as well as the sensitivity to model free-parameters. Our main results are presented in Section 4, which describes some representative fits and examines the spectral and latitudinal behavior of the parameters. Temporal changes are described in Section 5. In Section 6 we discuss and review the main results of this work, and compare our findings with previous studies.

2. Observations and data reduction

2.1. Observations

In Fig. 2 we show two typical sets of Saturn images taken in 1995 and 2002, in three different filters. There is a clear change of viewing geometry that allows us to observe the most southern latitudes but that also hides the northern ones. Light scattered and absorbed by gas and atmospheric particles is responsible for the visual appearance of the planet, organized in dark belts and bright zones.

Table 2 summarizes the observations we have used in this work. Most of them are fully described in Cuzzi et al. (2002) and French et al. (2003). These observations cover the five WFPC2 wideband UBVRI filters (F336W, F439W, F555W, F675W, and F814W) and occasionally the F255W, F785LP, FQCH4N, and F1042M filters. Archival data from other HST programs were employed to complete the spectral and temporal coverage (P.I. Beebe 1994, P.I. Tomasko 1995, P.I. Gerard 1997, and P.I. Biretta 2001). In Table 2 we also give the geometric quantities that define the observations. B is the sub-earth planetocentric latitude (or the ring opening angle at the Earth), B' the sub-solar planetocentric latitude (or the ring opening angle at the Sun) and α is the solar phase angle, defined as the Sun–Saturn–Earth angle. In Fig. 1 we show the variation of B' from 1975 to 2010. This includes our period of observation (from the southern spring equinox to the southern summer solstice) together with that of Pioneer 11, Voyager 1 and 2 and Cassini.

The characterization of each filter is given in Table 3, following the HST description given by Karkoschka (1998a) (http://www.stsci.edu/instruments/wfpc2/Wfpc2_phot/wfpc2_ss_phot.html). λ_m is the mean air-wavelength in nanometers, W is the width of the filter, defined as four times the average deviation; and A is the mean methane absorption coefficient. For the UV filters, two parameters are given, the first one for the first day after the last decontamination and the second one for thirty days after. Decontamination dates are given by the WFPC2 group (http://www.stsci.edu/instruments/wfpc2/Wfpc2_memos/wfpc2_decon_dates.html).

2.2. Data reduction and photometry

2.2.1. Image navigation

In order to navigate the images we employed the LAIA software (see, for example, Sánchez-Lavega et al., 2003; Sánchez-Lavega et al., 2002; García-Melendo and Sánchez-Lavega, 2001; Sánchez-Lavega et al., 2000), developed by J.A. Cano (Grup d'Estudis Astronomics, GEA, http://www.astrogea.org/soft/laia/laia.htm). First, we rotated the images by using the ring symmetry and then fitted the limb of the planet by means of a gradient-search technique. Once the center of the disk is found, the software can locate any point of the disk in terms of its latitude (either planetocentric or planetographic) and longitude (in any of the commonly used systems). Typical errors in location (latitude and longitude) are about $\pm 0.5°$. Problematic regions are polar latitudes or longitudes at more than $\pm 85°$ from the central meridian, but even at these locations the error is typically less than $\pm 1°$. To estimate the induced errors in the relevant scattering angles (μ, cosine of the emission zenith angle; μ_0, cosine of the solar incidence zenith angle; and $\Delta\phi$, the difference in azimuthal angles) we defined a smooth error function in both latitude and longitude that reproduced the observed uncertainties. This leads to relative errors in μ and μ_0 that are always under 5% (near the limbs) and typically on the order of 2%. The relative errors in $\Delta\phi$ were even smaller. Around the sub-earth and sub-solar point the relative errors in all the scattering angles were at their minimum, below 1%.

2.2.2. Photometric calibration

We used the standard pipeline-processed images and converted from data number (DN) to reflectivity (I/F). The reflectivity I/F is defined as the ratio of surface brightness I to that of a perfect, flat, Lambert surface at normal in-

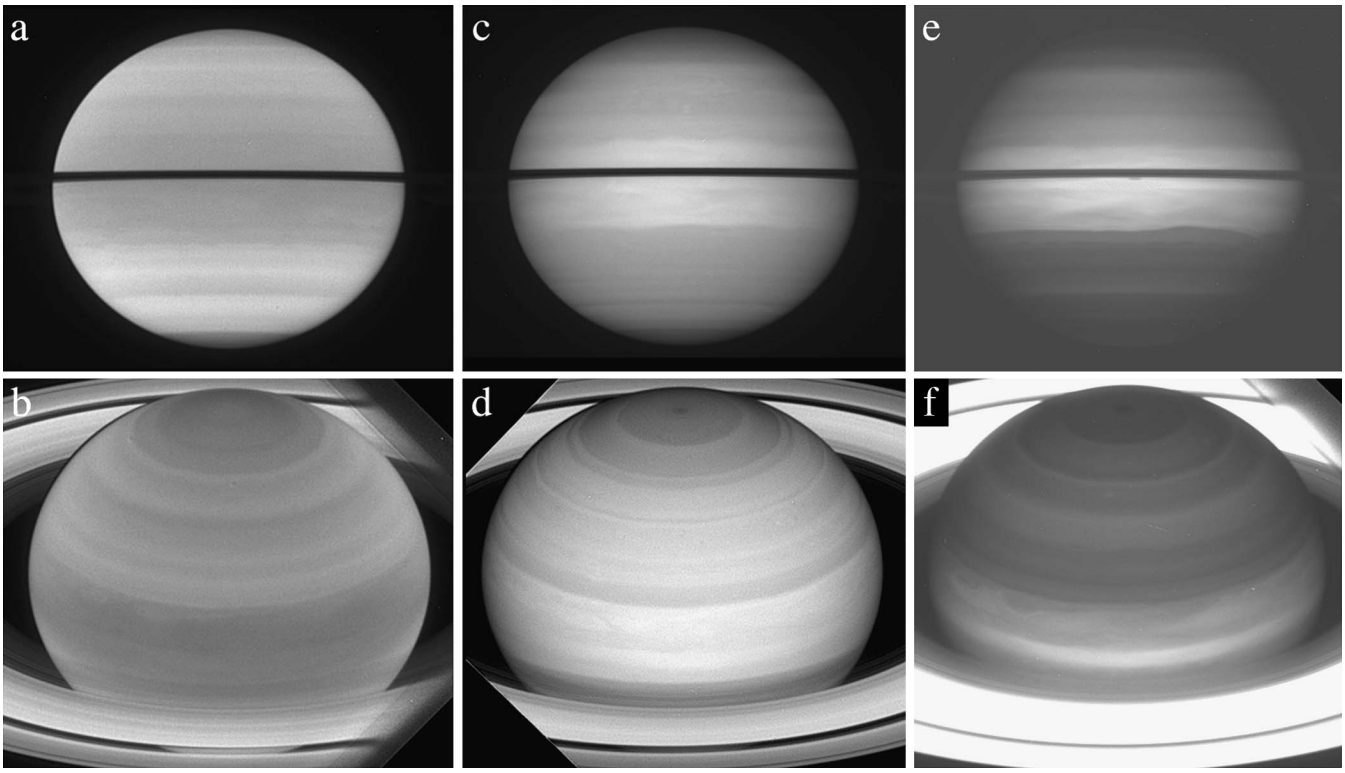

Fig. 2. HST Saturn images at selected wavelengths and years. The upper images (a, c, e) were taken in 1995 and the lower images (b, d, f) were taken in 2002. From left to right the filters are F336W (a, b), F673N and F675W (c, d), and FQCH4N (e, f). Note the inverse brightness at the equator (dark in F336W, bright in FQCH4N) and the hemispheric asymmetry in the upper panels.

cidence $\pi F(\lambda)/\pi$, where $\pi F(\lambda)$ is the solar irradiance at wavelength λ (Cuzzi et al., 2002).

For the French et al. (2003) data set, the DN to I/F conversion factor was obtained as described in Cuzzi et al. (2002), whereas for the rest of the images we employed the method described by Karkoschka (1998a) (http://www.stsci.edu/instruments/wfpc2/Wfpc2_phot/wfpc2_ss_phot.html). Both methods agree within a few percent for all filters and images, but we checked them using calibrated spectra of the rings (Barnet et al., 1992b; Poulet et al., 1999) whenever they were at a relatively large ring opening angle ($B > 15°$). We took into account the dependence of the UV filter throughput on the time since the most recent decontamination date, following the prescription of the WFPC2 team (http://www.stsci.edu/instruments/wfpc2/Wfpc2_memos/wfpc2_decon_dates.html).

We also computed the photometric effect of the ring reflectivity on the Southern Hemisphere in the 1994–2003 period for regions well removed from the ring shadow (which affected our 1994–1995 equatorial observations and indeed, prevented us from analyzing some regions). To estimate the ring-shine effect, we used a radiative model based on Barnet (1990), but with a different physical characterization of the ring, based on Dones et al. (1993). The ring-shine is strongest at southern summer solstice, and while it could affect the center-to-limb reflectivity variations, it is well below 5% of the absolute reflectivity, so its effects can be neglected for our purposes.

The systematic uncertainties that affect the photometric calculations include:

(1) those related to solar spectrum accuracy;
(2) those related to the filter plus system response functions (Karkoschka, 1998a); and
(3) filter peculiarities.

The first can be estimated with 1% and the second with 3% accuracy (Karkoschka, 1998a). This implies a raw total photometric accuracy of ∼5%. However, some filters show peculiar problems that increase this value. Correction from decontamination dates, or red leaks as in F336W (Cuzzi et al., 2002), vignetted fields as in FQCH4N (Karkoschka, 1998a) or anomalous results as in F1042M (Cuzzi et al., 2002) provide 10% or 15% accuracy as a reasonable estimate for these filters. Random errors arise because of the photon shot noise and are about 1%. Horizontal inhomogeneities in the hazes also cause dispersion around a mean reflectivity curve and can be treated as random errors, given that we are interested in the mean vertical structure, not in local variations of parameters. However, these random errors are insignificant for most filters except those in UV, where values can be as high as 3%. This is suggestive of a more locally variable atmosphere in the upper levels.

Table 2
Observations

Date	B	B'	α	Filters	Mode	ID	PI
1994/12/01	7.89	5.17	−5.83	F255W, F336W, F410M, F547M, F673N, FQCH4N, F953N	WF	5776	Beebe
1995/11/17	2.67	0.04	−5.42	F255W, F336W, F410M, F467M, F588M, F673N, FQCH4N, F953N	WF/PC	6030	Tomasko
1996/10/14	−3.82	−4.93	1.93	F336W, F439W, F555W, F675W, F814W	PC	6806	French
1997/01/10	−3.72	−6.24	5.67	F785LP	PC	6806	French
1997/09/11	−10.95	−9.84	3.14	F218W, F255W, FQCH4N	PC	6648	Gerard
1997/10/01	−10.28	−10.15	0.98	F785LP	PC	7427	French
1997/10/06	−10.12	−10.22	0.49	F336W, F439W, F555W, F675W, F814W, F1042M	PC	7427	French
1998/10/13	−15.57	−15.42	1.20	F336W, F439W, F555W, F675W, F814W, F1042M	PC	7427	French
1998/10/18	−15.43	−15.48	1.28	F255W	PC	7427	French
1999/11/03	−19.98	−20.16	0.42	F1042M	PC	8398	French
1999/11/07	−19.90	−20.20	0.30	F336W, F439W, F555W, F675W, F814W	PC	8398	French
2000/12/06	−23.33	−23.96	1.99	F255W, F336W, F439W, F555W, F675W, F814W, F785LP, F1042M	PC	8660	French
2001/09/08	−26.16	−25.71	6.37	F336W, F439W, F555W, F675W, F785LP, F814W	PC	8802	French
2001/09/28	−26.13	−25.80	5.95	FQCH4N	WF	9256	Biretta
2002/12/09	−26.52	−26.72	1.00	F255W, F336W, F439W, F555W, F675W, F814W, FQCH4N	PC	9341	French
2003/08/25	−25.41	−26.17	5.05	F255W, F336W, F439W, F555W, F675W, F814W, FQCH4N	PC	9809	French

Note. B—sub-earth planetocentric latitude; B'—sub-solar planetocentric latitude; α—phase angle.

2.2.3. *Photometric results*

In Fig. 3, we present North–South scans for several years and a selection of filters. The selection of years (1995, 1997, 1999, and 2002) offers a clear picture of both the geometrical variations and the observed evolution of the atmosphere. The temporal variation of reflectivity is apparent, especially in the equatorial region in the red filters (675 and 814 nm). Another example of very strong local variability is shown in Fig. 4. The reflectivity varied strongly, especially at 439 nm, around the 47° S planetographic latitude, changing from a positive contrast (brighter than its environment) to a neutral or even negative (darker) one. Such changes are frequent and especially clear in some filters like 439 nm or 814 nm, with time-scales from months to years.

In order to obtain preliminary information on the variation of reflectivity with latitude, we fitted our observations to a Minnaert limb-darkening model law (Tomasko et al., 1984):

$$I/F = (I/F)_0 \mu_0^k \mu^{k-1}, \quad (1)$$

Table 3
Filter description

Filter name	λ_m (nm)	W (nm)	A (1/km$_{am}$)
F218W	240	83	0.000
	242	87	
F255W	275	62	0.000
	276	62	
F336W	338	51	0.000
	338	51	
F410M	410	23.6	0.000
	410	23.6	
F439W	434	69	0.000
	434	69	
F467M	467.1	24.0	0.001
F547M	549	69	0.021
F555W	549	173	0.035
F588N	589.4	7.1	0.004
F673N	673.2	6.8	0.048
F675W	672	125	0.32
F785LP	867	192	3.5
F814W	798	218	1.8
F953N	954.5	7.5	0.37
F1042M	1022	58	6
FQCH4N	889.5	22.8	23

Note. λ_m—mean wavelength; W—width; A—methane absorption coefficient.

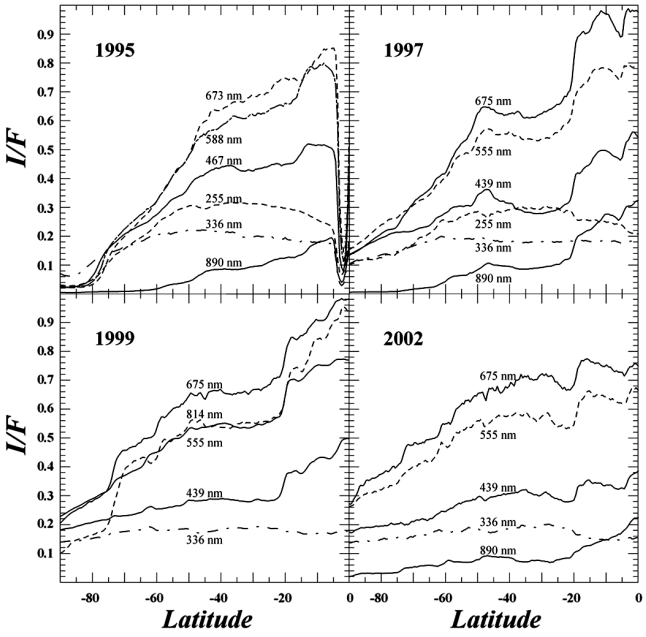

Fig. 3. North–South scans of absolute reflectivity at indicated wavelengths and years. We express the wavelength as the nominal wavelength of the filter. Note the presence of ring shadowing in the 1995 observations.

where $(I/F)_0$ is the reflectivity corrected for geometrical effects and k is the so-called Minnaert limb-darkening coefficient and they are obtained by a least squares fit for longitudes between ±80° from central meridian. From these fits, we gain some insight into the reflectivity changes and how they affect the limb-darkening behavior, although these results alone do not enable us to draw any conclusions about the vertical structure variations that lie behind such changes.

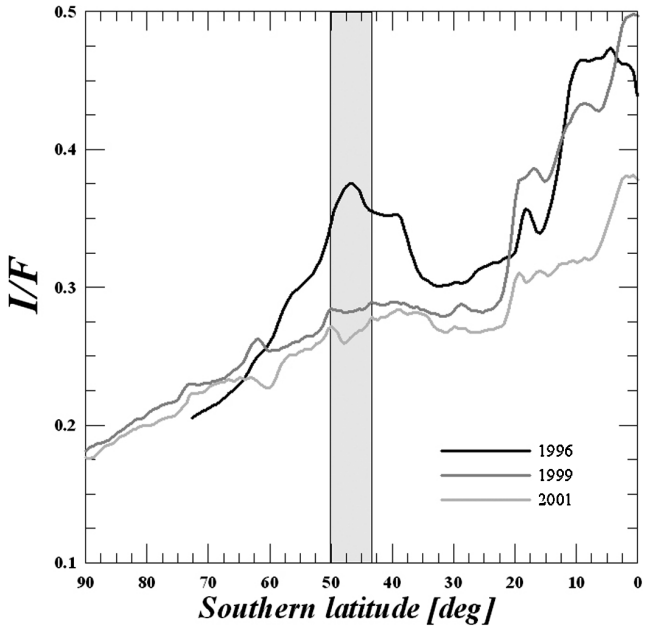

Fig. 4. A comparison of the observed equator to Pole reflectivity scans along the central meridian at 439 nm in 1996, 1999, and 2001 is shown. Note the strong darkening of the band centered at 47° S with respect to its surroundings.

In Fig. 5 we show the latitudinal dependence of Minnaert parameters for the same years as in Fig. 3 and for three important filters: F336W in the near-UV (available for all years), F675W together with the F673N (where Saturn is the brightest in our spectral range) and FQCH4N, which senses the tropopause level.

We see some clear latitudinal variations in these results. The Equatorial Zone is quite bright in the red filters, as known from previous studies (e.g., West, 1982). There is also a change of limb-darkening behavior at latitudes poleward of 60° S at 336 and 890 nm, the filters sounding the upper levels of the atmosphere. It is clear that, in these filters, there are changes in reflectivity with a variety of time scales, and that these changes also affect to the position of the reflectivity peaks. But in order to obtain a precise picture of what is happening in Saturn's atmosphere, we need a more detailed model of the atmospheric reflectivity that provides information of the vertical structure of the upper atmosphere.

3. Model description

3.1. Radiative transfer code

The radiative transfer code for atmospheric reflectivity employed in this work is fully described in Acarreta and Sánchez-Lavega (1999). It is based on the well-known "doubling–adding" technique of Hansen and Travis (1974). Our numerical model reproduces the center-to-limb variation of absolute reflectivity (I/F) at a given wavelength, assuming an atmospheric structure as described in the next

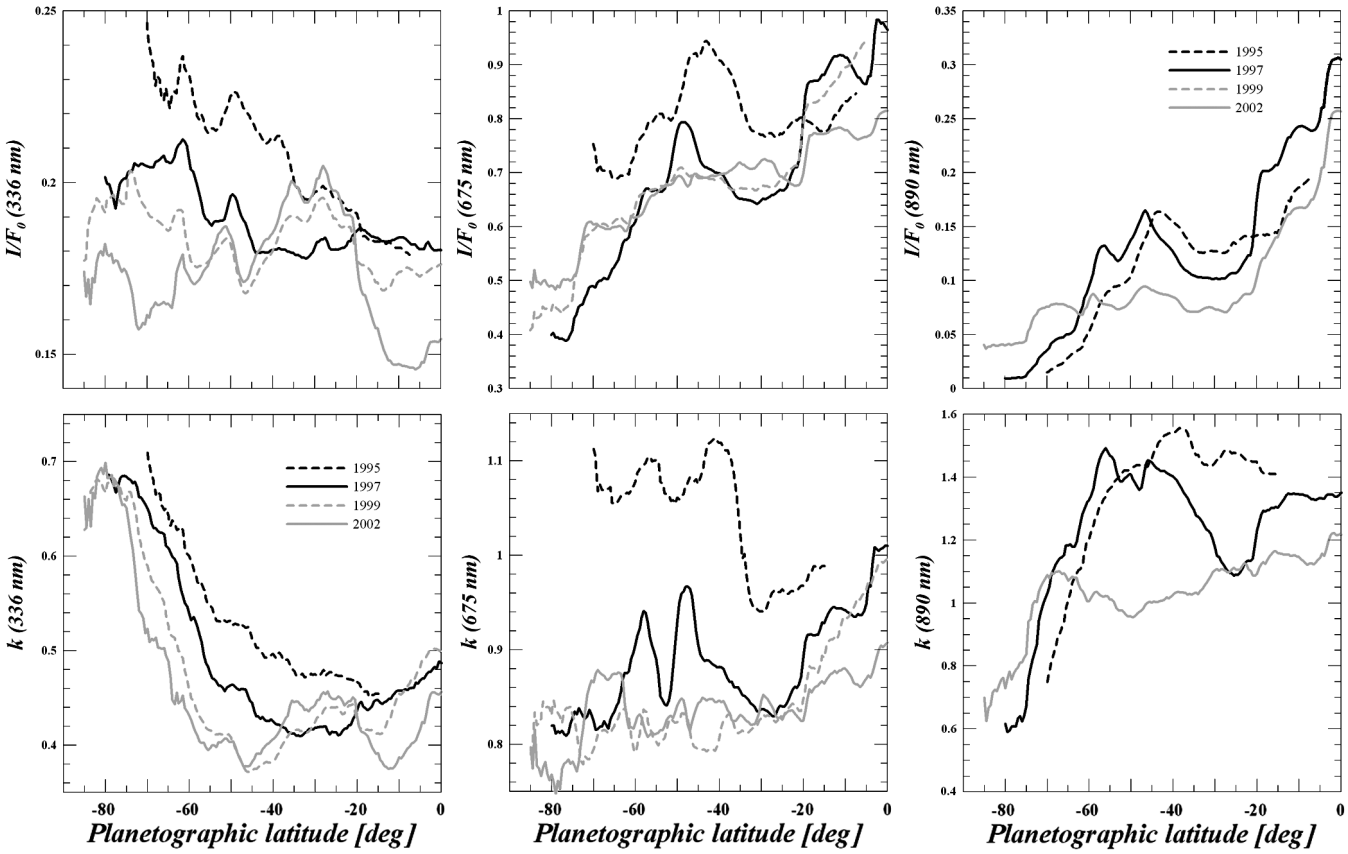

Fig. 5. Results of the Minnaert fitting for a selection of years and filters vs planetographic latitude. Dashed black line is used for 1995 results, continuous black or 1997, dashed gray for 1999 and continuous gray for 2002. Note the different scales for each wavelength.

section. It takes into account the effect of the gas, by means of scattering (H_2 and He) and absorption (CH_4). Layers of particles concentrated or mixed with the atmospheric gas can be incorporated by specifying their phase function, optical thickness and location. The model accommodates many phase functions, such as isotropic, Mie (van de Hulst, 1981) or double Henyey–Greenstein (Irvine, 1965). In order to reproduce layers that contain gas and particles, we take into account the scattering and absorption of both components by weighting phase functions with the optical thickness produced by each component, as explained, for example, in Liou (1992).

The methane mixing ratio by number relative to H_2 was taken as 0.003 (Karkoschka and Tomasko, 1992) with a mean molecular weight of 2.135 $\mathrm{g\,mol^{-1}}$ (Acarreta and Sánchez-Lavega, 1999). We assumed a mean methane absorption coefficient for each filter, as shown in Table 3 (Karkoschka, 1998a), independent of temperature and pressure. This is the coefficient yielding the observed average I/F over the filter bandpass (Karkoschka, 1998b). The vertical temperature profile is that of Lindal et al. (1985) and the equatorial gravity is 8.96 $\mathrm{m\,s^{-2}}$ varying with latitude due to Saturn's oblateness and rotation.

Our code neglects polarization, performing a scalar solution of the radiative transfer equations. Although it does not take into account any dynamical effects, the study of observations taken at different times allows a temporal characterization of the upper clouds and hazes. We considered all clouds to be horizontally infinite and that the particles scatter light independently of each other. It is also based on the plane-parallel approximation, which induces some errors at extreme viewing angles (Ortiz et al., 1996). We have excluded observation points with angles of incidence or scattering greater than 70° (i.e., $\mu, \mu_0 > 0.342$).

Another approximation is the use of the mean wavelength for each filter as defined in Table 3. The validity of this approach depends on the width of the filter and the dependence of the different atmospheric properties with wavelength over the selected spectral range. For narrow filters, the mean methane absorption coefficient is the effective absorption coefficient, but for wide filters, it is only an upper limit to the effective absorption coefficient (Karkoschka, 1998a). This is good enough for our purposes, as long as the deep methane band filter employed is very narrow. Other filters including methane bands will overestimate methane absorption but a carefully control with the 890 nm filter prevents significant deviations in the results.

3.2. Basic atmosphere model

We show in Fig. 6 our basic atmosphere model, similar to that of Ortiz et al. (1996) and Muñoz et al. (2004). We as-

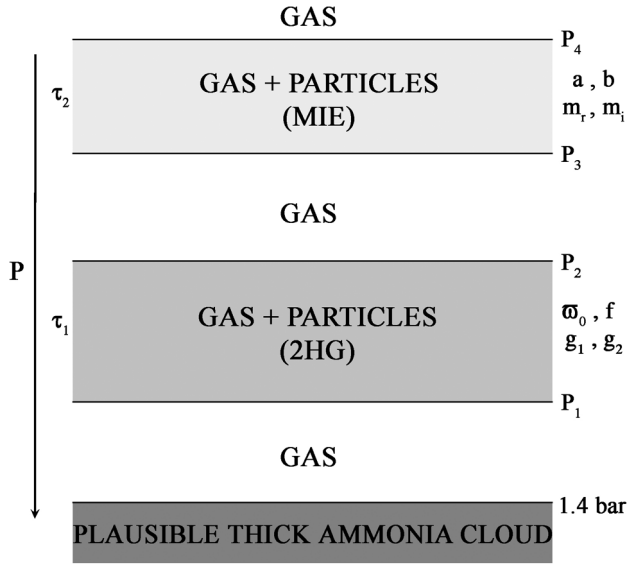

Fig. 6. Basic vertical model structure free parameters. The pressure increases downwards. For each layer we show whether it contains particles or not, and the phase function and parameters used.

sume that there are two layers of particles and a semi-infinite cloud at the bottom, putatively formed by ammonia ice. This first layer is thus "white," in the sense of no absorption, and scatters isotropically, because of its thickness. As we show below, its effect on the final results is very small. This three-layer model has been extensively used, as the polarization measurements of Pioneer 11 did not agree with a single layer of scatterers (Danielson and Tomasko, 1969). More recently, Stam et al. (2001) also found this kind of structure, with two clear regions.

The tropospheric haze extends from a level close to the tropopause (P_2) to an intermediate level (P_1) located above the ammonia cloud (Stam et al., 2001). For this second layer we used a two-term Henyey–Greenstein function

$$P(\theta) = f \cdot p(g_1, \theta) + (1 - f) \cdot p(g_2, \theta), \tag{2}$$

where

$$p(g, \theta) = \frac{1 - g^2}{\sqrt{1 + g^2 - 2g\cos(\theta)}}. \tag{3}$$

This phase function is based on the widely-used Henyey–Greenstein function (Henyey and Greenstein, 1941), which has a mathematically attractive form but whose relationship to the physical parameters of the scattering particles is not clear. The double Henyey–Greenstein phase function is well suited for the tropospheric particles as shown in Tomasko and Doose (1984). Parameter g_1 is called the forward scattering asymmetry factor and g_2 the backscattering one. Parameter f is the relative weighting factor between them. The two last parameters needed for the tropospheric haze are the optical thickness (τ_1) and the single scattering albedo $\overline{\omega}_0$, an indication of the particles absorption, with $\overline{\omega}_0 = 1$ for perfectly scattering particles and $\overline{\omega}_0 = 0$ for perfect absorbers.

Table 4
Model parameters initial ranges and wavelength dependency

	Parameter	Wavelength dependent	Initial range	References
Tropospheric haze	P_1	No	200–800 mbar	S01
	P_2	No	50–150 mbar	S01
	τ_1	–	0–100	O96
	$\overline{\omega}_0$	Yes	0.7–1.0	K&T93
	f	–	0.5–0.9	T&D84
	g_1	–	0.6–0.8	T&D84
	g_2	–	−0.2–−0.4	T&D84
Stratospheric haze	P_3	No	1–30 mbar	S01
	P_4	No	10–50 mbar	S01
	τ_2	Yes	0–1	K&T93
	m_r	–	1.33–1.55	KT93
	m_i	Yes	−0.001–−0.5	KT93
	a	No	0.1–0.25 μm	O96
	b	No	0.05–0.2	O96

Note. S01—Stam et al. (2001); O96—Ortiz et al. (1996); K&T93—Karkoschka and Tomasko (1993); T&D84—Tomasko and Doose (1984).

The upper, third, layer is located at the stratosphere, between pressures P_3 and P_4. This haze is supposed to be formed by small particles (e.g., Karkoschka and Tomasko, 1993). We used a Mie phase function, characterized by the real and imaginary refractive index of the particles (m_r and m_i) and a particle size distribution $\eta(r)$. In this case, we employed that of Hansen and Travis (1974)

$$\eta(r) = r^{(1/b-3)} e^{-r/ab}, \tag{4}$$

where a is an estimation of the effective radius and b can be interpreted as a measurement of the deviation from this value. A small particle size implies that the optical thickness τ_2 is expected to be strongly dependent on wavelength (Hansen and Travis, 1974), decreasing from UV to IR, as we will discuss below.

Table 4 shows our initial ranges for model parameters, together with their wavelength dependent behavior, based on the main references listed. For some parameters (marked "–") the wavelength dependence is unclear, or we preferred not to make any initial assumptions about it.

3.3. Fitting strategy and sensitivity to model parameters

To quantify the quality of our model calculations, we define a mean quadratic deviation between the observation and model prediction, as in West (1983)

$$\chi^2 = \frac{1}{N} \cdot \sum_{i=1}^{N} \left\{ \frac{1}{\sigma_i^2} \cdot \left[R_\mathrm{obs}(\mu_i, \mu_{0i}, \Delta\phi_i) - R_\mathrm{mod}(\mu_i, \mu_{0i}, \Delta\phi_i) \right]^2 \right\}. \tag{5}$$

In Eq. (3), N is the number of points to be fitted by the model (i.e., the number of points in the longitudinal scan); σ_i is the error in the ith measurement; R_obs is the observed and R_mod the modelled reflectivity at point $(\mu_i, \mu_{0i}, \Delta\phi_i)$.

Table 5
Relative random errors of model parameters

Filter	P_1	P_2	τ_1	$\bar{\omega}_0$	f	g_2	τ_2	m_r	m_i	a
218	0.20	–	–	0.05	0.20	–	0.20	0.05	0.15	0.20
255	0.15	–	–	0.05	0.10	–	0.20	0.05	0.15	0.10
336	0.05	–	0.25	0.05	0.05	0.15	0.10	0.05	0.20	0.05
439	0.25	–	–	0.01	0.05	0.10	0.25	0.15	–	0.15
555	–	–	–	0.01	0.05	0.05	–	–	–	–
675	–	–	–	0.01	0.05	0.05	–	–	–	–
785	0.05	0.10	0.10	0.01	0.05	0.05	–	–	–	–
814	0.10	0.15	0.10	0.01	0.05	0.05	–	–	–	–
890	0.05	0.25	0.10	0.01	0.10	0.15	–	–	–	–
1042	0.10	0.25	0.20	0.01	0.10	0.10	–	–	–	–

Note. This table gives the relative change needed in each parameter to obtain a substantial deviation in the model calculation obtained at a given wavelength. Thus, it is an expression of the relative error of the model parameters.

The value of the random error σ_i is 1–3%, as previously explained. If we obtain $\chi^2 < 1$ for our model we can assure that there is no statistically significant deviation from observed values.

If we convert the estimated uncertainties in the scattering angles μ, μ_0, and $\Delta\phi$ to an uncertainty in the modelled reflectivity, we always find combined errors below ∼2%. To account for these geometrical uncertainties, we ignored longitudes farther than ±80° from the central meridian and compared results from ±1° in latitude with the latitude under consideration.

We selected 20 latitudes to characterize the whole Southern Hemisphere by inspecting the North–South reflectivity curves and the images in all filters. This discretization covers all observed variations in reflectivity from equator to pole in all wavelengths and years. Given a latitude and date, our goal is to fit the observed reflectivity at all wavelengths simultaneously. To do so, we try to minimize the χ^2 function in the free-parameter space.

We first analyzed observations from 2002 by scanning the free-parameter space at high resolution. We performed ∼50 000 simulations to constrain the properties of atmospheric particles and limit as much as possible the number of free parameters. As a result of these initial studies, we decided to fix some model parameters. Results showed small sensitivity to g_1 and b, so we fixed them at $g_1 = 0.7$ and $b = 0.1$. We also found that the parameters defining the stratospheric haze (P_3, P_4, and τ_2) were strongly correlated, so we fixed, $P_3 = 10$ mbar and $P_4 = 1$ mbar (Stam et al., 2001), to make sure that the optical thickness varied between the expected values.

Once all the latitudes were fitted for 2002, we applied a revised fitting procedure. For every year's observations, we used the 2002 results as an initial guess. Parameters P_2 and τ_1 are very well constrained by the deep methane-band filter observations. After fitting them using these two parameters, we fitted from UV observations (sounding upper levels) to near-IR observations (sounding lower levels). We followed a nested loop sequence in which more parameters were added (from the most to the least sensitive) if no satisfactory fit was found. For example, in the UV filters (typically F255W or/and F336W) we fitted the stratospheric particle properties (τ_2, m_r, m_i, a) and then, if no acceptable fit was found ($\chi^2 < 1$) we revised the tropospheric parameters (P_2, τ_1, $\bar{\omega}_0$). Whenever a substantial revision of the initial parameters was required, the fitting process started again from the methane observations. Once this step was completed we moved to the visible and near-IR filters in a similar fashion. Table 5 provides an indication of the sensitivity of the observations in each filter to the model parameters, and thus of the hierarchy of parameters as each filter was fitted. This strategy converged quite rapidly to a low χ^2 fit. We checked the sensitivity of our procedure to the choice of initial parameters and found no significant deviations in the final fitted parameters, but an increase of the computational time.

3.3.1. *Sensitivity to model parameters*

Random errors in the observations limit the accuracy of the values obtained for the model parameters. Table 5 shows the relative variation needed in each model parameter to obtain a significant deviation (1%, 5%, 10%, 15%, 20%, 25% or, larger than 25%) from the best-fitting model.

We also tested the effect of the systematic photometric errors on the model results by fitting the reflectivity curves displaced by 5% or 10% (depending on the filter, as explained above) up and down. Systematic errors are larger than the random ones but they preserve the limb darkening information so they do not affect all parameters equally. The most significant effect (an increase from ∼10% to 20–25%) is found in the top pressure P_2 and optical thickness τ_1 of the tropospheric haze. The real refractive index m_r is also increased from 10% to 20%. Using these values together with those in Table 5, we have a good indication of the errors in our model parameters.

4. Results

4.1. *Mean properties*

In Table 6, we present the values of the parameters that produce the best fits for three particular years (1995, 1999, and 2002) at three representative latitudes: 6° S for the Equatorial Zone, 36° S for the southern mid-latitudes and 73° S for the Southern Polar Region. Note that, because of Saturn's rotational axis tilt, of 1995 data we analyzed 10° S instead of 6° S and 63° S instead of 73° S.

Fig. 7 shows the latitude brightness scans and the best fitting models for the cases shown in Table 6. Some of the challenges in modelling the observations (e.g., the absence of observations in the methane or incomplete coverage of the disk of the planet) are clear in this figure. However, we are confident that we have overcome these challenges and that we have accurate determinations of atmospheric properties.

Table 6
Best fitting parameters for 1995, 1999, and 2002

λ_{nom} (nm)	τ_1	ϖ_0	f	$\lvert g_2\rvert$	τ_2	m_i	τ_1	ϖ_0	f	$\lvert g_2\rvert$	τ_2	m_i	τ_1	ϖ_0	f	$\lvert g_2\rvert$	τ_2	m_i
1995	10° S						36° S						63° S					
255	45	0.7	0.9	0.3	0.5	0.008	18	0.7	0.8	0.3	0.75	0.008	5	0.65	0.95	0.3	0.25	0.03
336	45	0.7	0.85	0.3	0.4	0.001	20	0.7	0.85	0.3	0.29	0.001	5	0.7	0.9	0.3	0.19	0.001
410	45	0.88	0.7	0.2	0.33	0.001	20	0.845	0.7	0.3	0.24	0.001	5	0.8	0.7	0.3	0.19	0.001
467	45	0.963	0.7	0.2	0.35	0.001	20	0.955	0.7	0.25	0.21	0.001	5	0.901	0.7	0.3	0.18	0.001
588	45	0.993	0.7	0.25	0.3	0.001	20	0.988	0.65	0.25	0.23	0.001	5	0.951	0.7	0.3	0.2	0.001
673	45	0.995	0.7	0.25	0.2	0.001	25	0.995	0.7	0.2	0.25	0.001	5	0.961	0.7	0.3	0.2	0.001
890	40	1.0	0.6	0.3	0.05	0.001	18	1.0	0.6	0.3	0.01	0.001	2.1	1.0	0.6	0.3	0.015	0.001
953	13	1.0	0.8	0.1	0	0.001	8.8	1.0	0.8	0.1	0.23	0.001	1.9	1.0	0.8	0.1	0	–
	$P_1 = 0.5$ bar, $m_r \sim 1.5$,			$P_2 = 60$ mbar $a \sim 0.2$ μm			$P_1 = 0.5$ bar, $m_r \sim 1.5$,			$P_2 = 80$ mbar $a \sim 0.2$ μm			$P_1 = 0.4$ bar, $m_r \sim 1.45$,			$P_2 = 110$ mbar $a \sim 0.15$ μm		
1999	6° S						36° S						73° S					
336	15	0.7	0.81	0.3	0.21	0.001	9	0.7	0.94	0.3	0.36	0.001	5	0.7	0.8	0.3	0.15	0.05
439	15	0.945	0.7	0.25	0.13	0.001	9	0.845	0.7	0.3	0.07	0.001	5	0.819	0.7	0.3	0.15	0.001
555	15	0.989	0.7	0.35	0.15	0.001	9	0.961	0.7	0.35	0.05	0.001	5	0.939	0.7	0.3	0.10	0.001
675	20	0.999	0.7	0.35	0.13	0.001	9	0.986	0.7	0.35	0.04	0.001	5	0.973	0.7	0.3	0	–
785	20	1.0	0.6	0.4	0.13	0.001	9	0.995	0.6	0.4	0	–	5	0.965	0.6	0.32	0	–
814	20	1.0	0.6	0.4	0.21	0.001	9	0.991	0.6	0.35	0	–	5	0.967	0.6	0.2	0	–
1042	20	1.0	0.6	0.35	0.11	0.001	7.7	1.0	0.6	0.4	0.1	0.001	3	1.0	0.6	0.25	0	–
	$P_1 = 0.3$ bar, $m_r \sim 1.45$,			$P_2 = 45$ mbar $a \sim 0.2$ μm			$P_1 = 0.35$ bar, $m_r \sim 1.5$,			$P_2 = 75$ mbar $a \sim 0.2$ μm			$P_1 = 0.4$ bar, $m_r \sim 1.45$,			$P_2 = 110$ mbar $a \sim 0.1$ μm		
2002	6° S						36° S						73° S					
255	18	0.7	0.9	0.3	0.5	0.01	7	0.7	0.8	0.3	0.7	0.01	5	0.7	0.95	0.3	0.25	0.2
336	20	0.7	0.95	0.3	0.3	0.001	7	0.7	0.9	0.3	0.3	0.001	5	0.7	0.9	0.3	0.16	0.01
439	20	0.898	0.7	0.25	0.1	0.001	7	0.862	0.7	0.35	0.05	0.001	5	0.754	0.7	0.3	0.09	0.001
555	20	0.980	0.7	0.3	0.06	0.001	7	0.961	0.7	0.4	0.08	0.001	5	0.938	0.7	0.3	0.09	0.001
675	20	0.994	0.7	0.3	0.0	–	7	0.992	0.7	0.35	0.01	0.001	5	0.976	0.7	0.3	0.07	0.001
814	20	0.999	0.6	0.3	0.04	0.001	7	0.999	0.6	0.358	0.03	0.001	5	0.996	0.6	0.3	0.12	0.001
890	18.2	1.0	0.6	0.3	0.03	0.001	6.4	1.0	0.6	0.3	0.05	0.001	4.3	1.0	0.6	0.3	0.03	0.001
	$P_1 = 0.4$ bar, $m_r \sim 1.5$,			$P_2 = 40$ mbar $a \sim 0.2$ μm			$P_1 = 0.35$ bar, $m_r \sim 1.5$,			$P_2 = 75$ mbar $a \sim 0.2$ μm			$P_1 = 0.4$ bar, $m_r \sim 1.45$,			$P_2 = 90$ mbar $a \sim 0.1$ μm		

4.1.1. The stratospheric haze

The stratospheric haze particles are small, with sizes ranging between 0.1 and 0.25 μm. The optical thickness thus decreases from the UV ($\tau_2 \sim 0.6 \pm 0.15$) to the IR ($\tau_2 \sim 0.05 \pm 0.05$), as expected (Hansen and Travis, 1974). With respect to their refractive indexes m_r and m_i, there is a strong latitudinal variation that will be analyzed in Section 4.2.1. Stratospheric particles are always UV-absorbers, as seen primarily at F255W ($m_i \leqslant -0.01$), with an increased absorption at the polar latitudes. Their real refractive index varies between 1.45 and 1.55.

In Fig. 8 both τ_2 and $|m_i|$ in the year 2003 for three selected latitudes are plotted. The latitudinal variations are clear and point to different generation processes.

4.1.2. The tropospheric haze

The tropospheric haze is primarily responsible for the visual appearance of the planet in the observed spectral range. It is thus very important to retrieve its properties accurately. The tropospheric haze optical thickness is only weakly dependent on wavelength. This dependence could be real (if the particles size were of the same order as the wavelength) or due to a differential vertical distribution (if the particles were much bigger than the wavelength) because the UV and deep methane filters are expected to sense an upper, less dense, level than the continuum filters.

The optical properties of the particles located in the troposphere are very different from those expected for fresh ammonia ice, so it is supposed that some additional or new species is present. The particles absorb strongly in the 200–300-nm region and then increase their single scattering albedo from the UV to the IR, where they are expected to be perfectly scattering particles.

There is also a clear wavelength dependence of parameter f from the UV to the IR, but it can be compensated by the values of the single scattering albedo $\bar{\omega}_0$. As shown in Fig. 9, maximum f variability (0.6–0.95) provides $\bar{\omega}_0 = 0.7$ at UV wavelengths, whereas minimum f variability (0.6–0.75) results in darker particles ($\bar{\omega}_0 < 0.6$) at shorter wavelengths. The values of parameters g_1 and g_2 show no significant trend and are close to the initial assumed values.

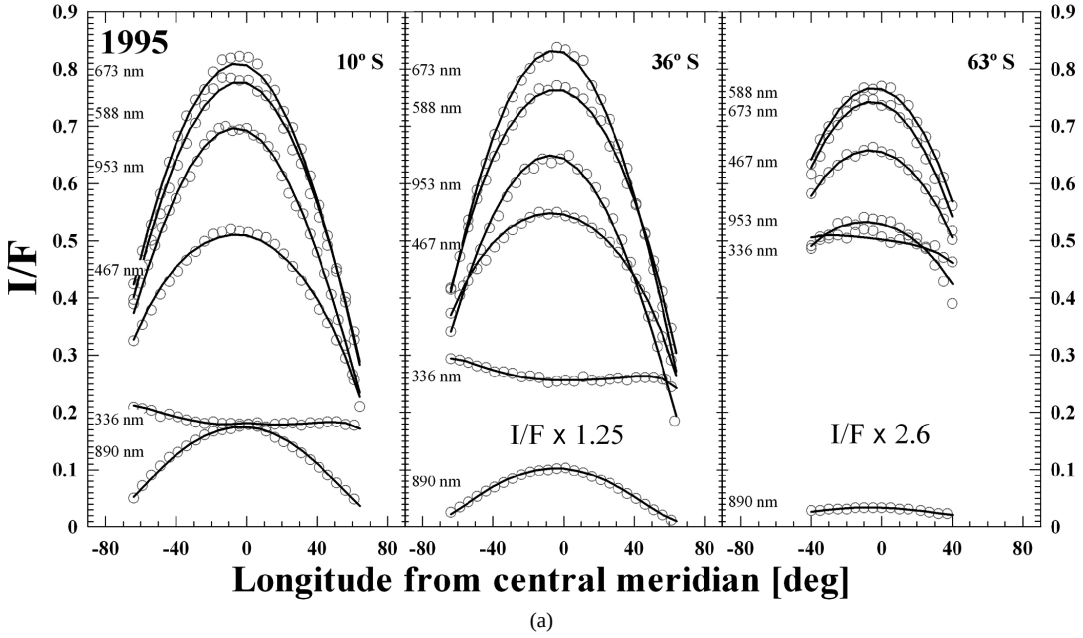

(a)

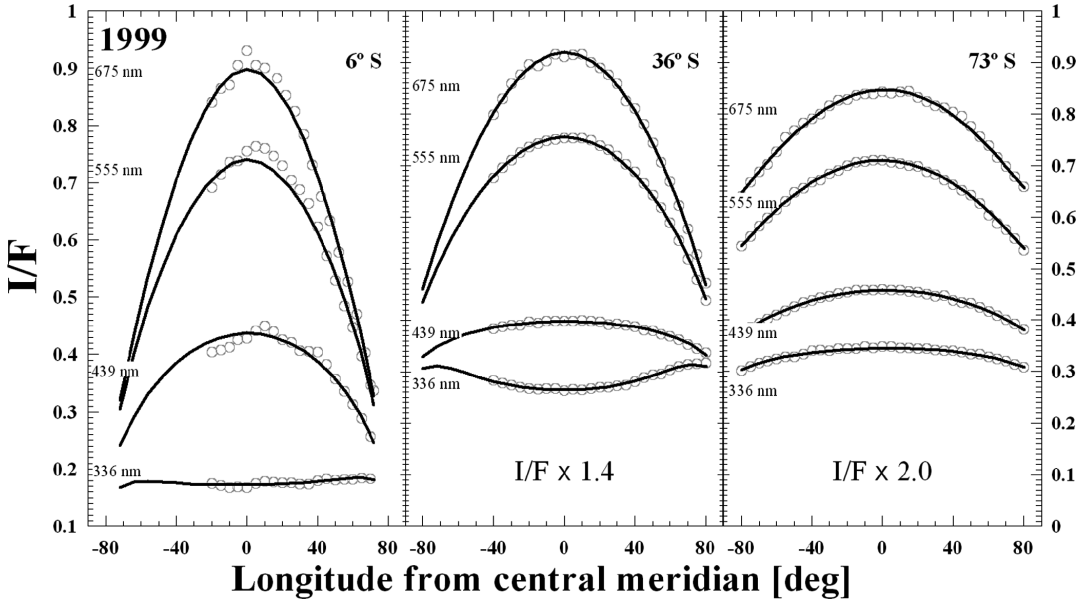

(b)

Fig. 7. East–West scans of absolute reflectivity at indicated latitudes, years and wavelengths. Grey circles show averaged data and the model results are plotted as a solid line. The plots are restricted to the range of longitudes for which it is acceptable to make a plane-parallel approximation. Note that the scale changes for each year, that the latitudes for 1995 are not the same because of geometry and that some of the plots show the reflectivity increased by a given factor. Panels (a), (b), and (c) show results from 1995, 1999, and 2002, respectively.

4.2. Latitudinal variations

A look at Saturn's images (see Fig. 2) shows that the planet can be broadly divided into three different regions, according to their visual appearance: the equator, the mid-latitudes, and the polar region. In terms of our model, this division is based primarily on the properties of the tropospheric haze (optical thickness and height), but also on the kind of stratospheric particles found at the pole. Altitude increases of the upper level of the hazes can be seen as darker regions in the 336 nm filter (a, b) that are brighter in the methane filter (e, f), like at the equator. This is caused by the competing effect of the Rayleigh scattering and particle absorption at the shorter wavelengths and the particle scattering and methane absorption in the longer ones. But there are other latitudinal differences in both hazes that are not so evident.

4.2.1. Stratospheric haze

There is a clear latitudinal variation in the stratospheric particles, as shown in Fig. 10. Particles are undoubtedly different southward of ∼68° S. There, particles are smaller

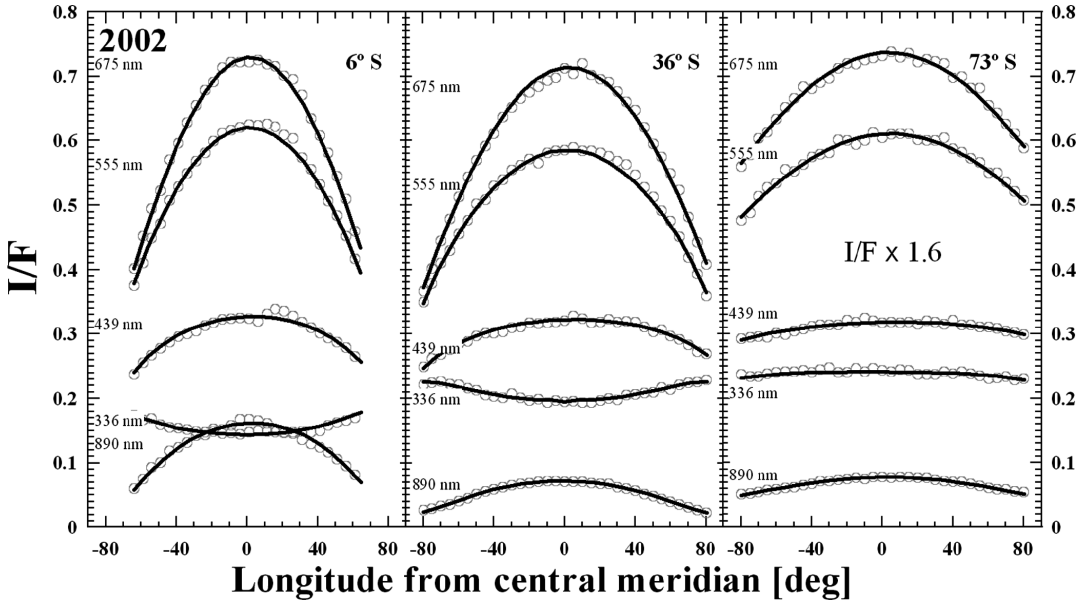

(c)

Fig. 7. Continued.

(0.1 μm) and more absorbent at UV wavelengths. Moreover, the real refractive index changes from $m_r \sim 1.5$ at mid-latitudes to $m_r \sim 1.45$ at the pole. At other latitudes, the particle properties are similar, although the mean particle radius in the middle latitudes is usually greater than at the equator where it is ∼0.1–0.15 μm.

The stratospheric optical thickness seen at shorter wavelengths follows a different pattern than at other wavelengths. Whereas the blue and red filters show a minimum at the middle latitudes, at UV (255 and 336 nm) the optical thickness of the stratospheric haze is larger. The profile shown in Fig. 10a is quite representative.

4.2.2. Tropospheric haze

The most important latitudinal variations take place in the tropospheric haze. Fig. 11 shows the strong decrease in optical thickness from equator to the pole, in 1995 and 2002, together with the variation of the single scattering albedo at different wavelengths in 1998. Latitudinal variations in both parameters are obvious and far above the modelling errors.

With respect to the properties of the tropospheric particles, there is a clear tendency to find darker particles at more southern latitudes (see Fig. 10). This effect is most noticeable at 439 nm, a very sensitive wavelength to all changes related to this parameter.

The pressure top level P_2 and especially the optical thickness vary strongly with latitude, being the most important factor generating the visual appearance of the planet. Fig. 12 shows the situation for the 2002 observations. For all years, we find a thicker and higher haze close to the equator (latitudes $<16°$ S), extending for more than two scale heights. Poleward of this equatorial region, the haze abundance (shown in Fig. 12 as the optical thickness per scale height) is sharply reduced. In the polar region, the tropospheric haze diminished to only one tenth of its equatorial abundance. Karkoschka and Tomasko (1993) related the latitudinal variations in the optical thickness per unit of height with the zonal wind profile, but we have not found this correlation. There are strong temporal variations in this parameter that will be further discussed in the following section.

Once we reach the 400–600 mbar level, in consequence of the large optical depth, our method based on visual and adjacent wavelengths broadband photometry starts to show a greater uncertainty. The bottom level of the tropospheric haze shows a weak trend of a higher pressure at lower latitudes, producing a descending haze with latitude. With respect to the ammonia cloud the conclusions are weaker; and longer wavelength observations, such as far-IR or radio (where tropospheric particles will give a lower optical depth), are needed.

In short, two different kinds of latitudinal changes have been found. On the one hand, stratospheric particles are intrinsically different at the pole: smaller, more absorbent at near-UV and with a different real refractive index. On the other hand, tropospheric particles are substantially the same but change their abundance and location. This is an important conclusion that could improve our knowledge about the origin of the haze particles.

5. Temporal evolution

Our long-term study enables us to search for temporal variations in the vertical structure of Saturn's clouds. We do know that such changes occur on Saturn (see Figs. 3 and 4). There are hemispherical differences, most easily observed at the ring plane crossing epoch (see Fig. 2), and,

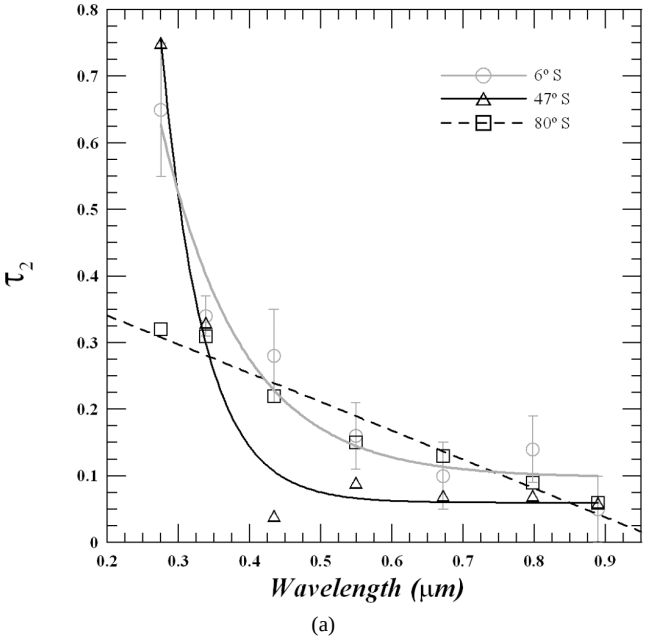

(a)

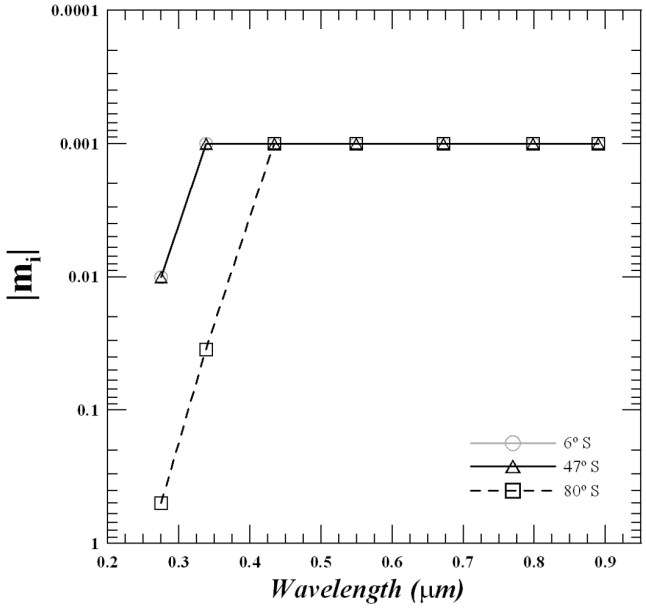

(b)

Fig. 8. The variation of the optical thickness τ_2 (a) and the imaginary refractive index m_i (b) of the stratospheric particles. Exponential (6° S and 47° S) and linear (80° S) fits are shown for τ_1. Note that polar particles are 'redder,' and have a very different spectral behavior. Error bars for τ_1 at 6° S are also shown.

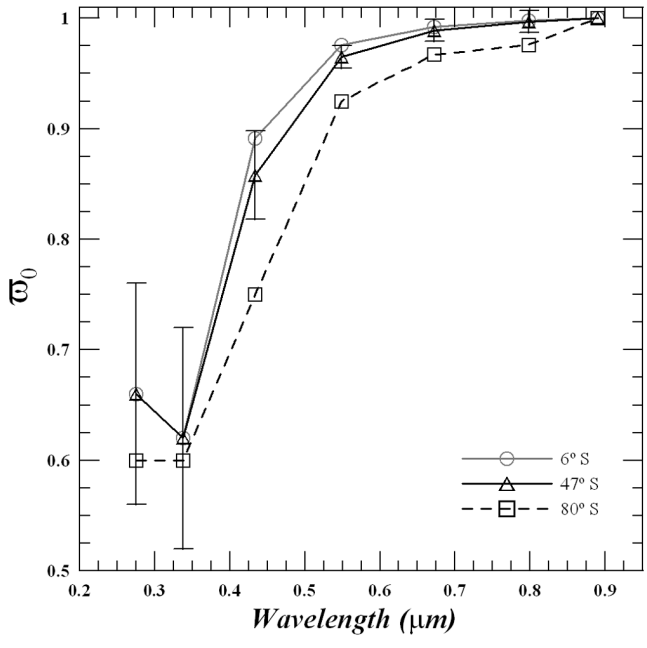

(a)

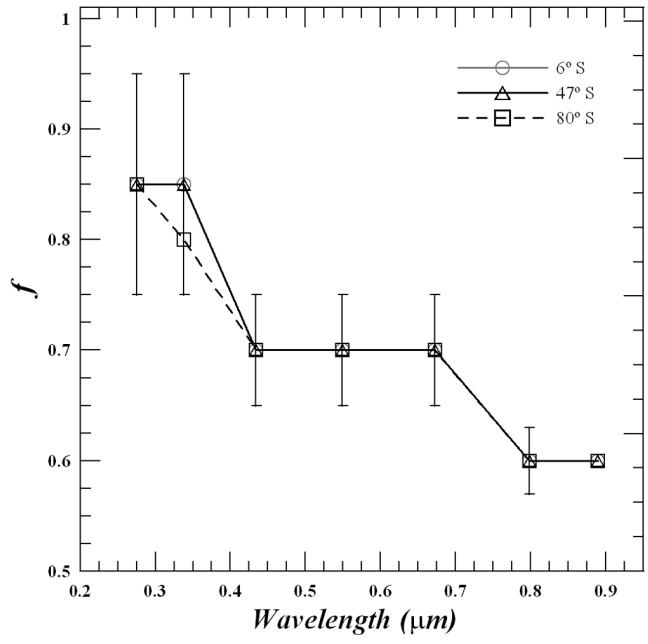

(b)

Fig. 9. Similar to Fig. 8 but for the single scattering albedo $\bar{\omega}_0$ (a) and parameter f (b) of the tropospheric particles with wavelength for year 2003 at three representative latitudes. Polar particles (poleward of ~70° S) are slightly darker than at other latitudes.

in addition, there are Great White Storms, known to occur mainly at the equator, that substantially affect the vertical cloud structure (Acarreta and Sánchez-Lavega, 1999). The first are usually related to seasonal variations in insolation associated with Saturn's obliquity and eccentricity (as shown in Saturn's seasonal cycle shown in Fig. 1), whereas the second have a dynamic origin, not necessarily bounded to the upper weather layer (Sánchez-Lavega and Battaner, 1986; Hueso and Sánchez-Lavega, 2004).

We chose to analyze a full hemisphere over a third of a seasonal cycle, rather than simply to look for differences in North–South reflectivity. Over this period, one might expect that the atmosphere would change from a "winter" structure to a "summer" one, with possibly superimposed dynamical variations.

The first question is to determine where the changes in cloud properties are located. As we have seen from the ver-

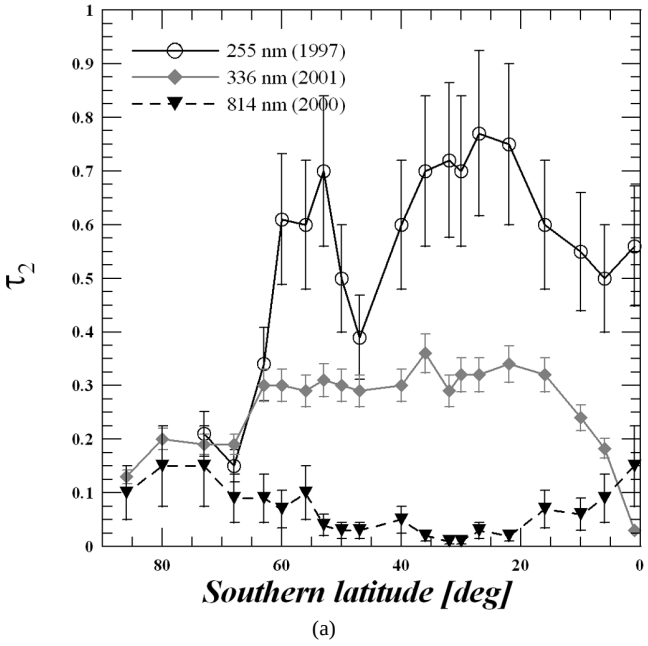

(a)

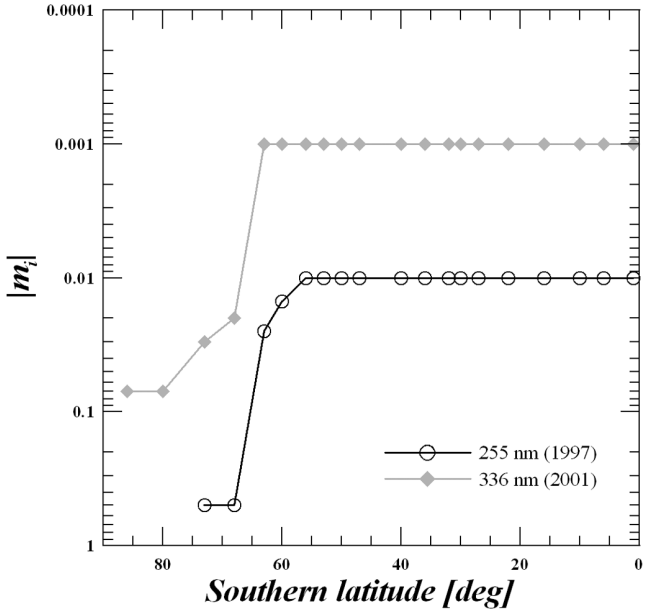

(b)

Fig. 10. Latitudinal behavior of the same parameters as in Fig. 8 (τ_2 (a) and m_i (b)) at three different wavelengths. There is an abrupt change southward of 60° S which marks the polar region. Greater optical thicknesses at short wavelengths are usually correlated with lower optical thicknesses at longer ones.

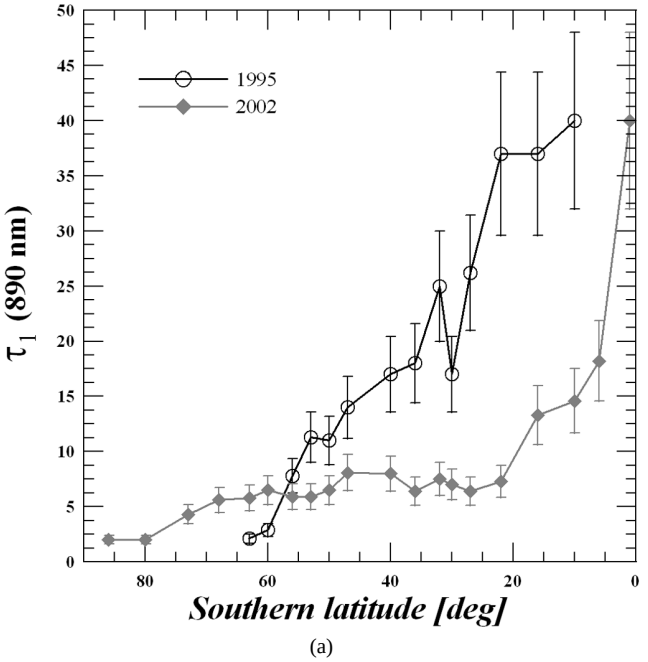

(a)

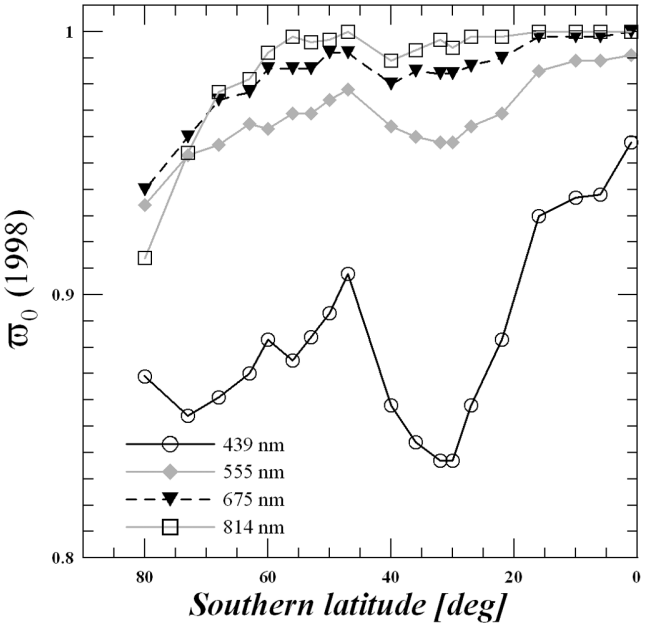

(b)

Fig. 11. Latitudinal behavior for 1995 and 2002 of the optical thickness and single scattering albedo of the tropospheric haze at different wavelengths. Strong latitudinal variations in the optical thickness are evident (a). The particles also brighten with increasing wavelength, but local changes at some wavelengths can be greater (b). For typical $\bar{\omega}_0$ errors see Fig. 9.

tical models presented so far, the visual appearance of the planet is most strongly affected by the tropospheric haze, so if we are actually seeing the changes, they are probably at the tropospheric levels. But one might expect greater variability in the stratospheric haze, because of its shorter radiative time constant associated with control by solar radiation.

The second important question is how the clouds change. A smooth change is expected if the geometrical parameters are pre-eminent, following the insolation changes, in accordance with the characteristic response time of the atmosphere. Of course, if the changes are due to dynamical effects, such as those that possibly developed after the equatorial stormy phenomena of 1990 and 1994, the observed results could be extremely fast or abrupt. Although we do not have continuous coverage over the period of our observations, ours is the first study enabling a search for long-term

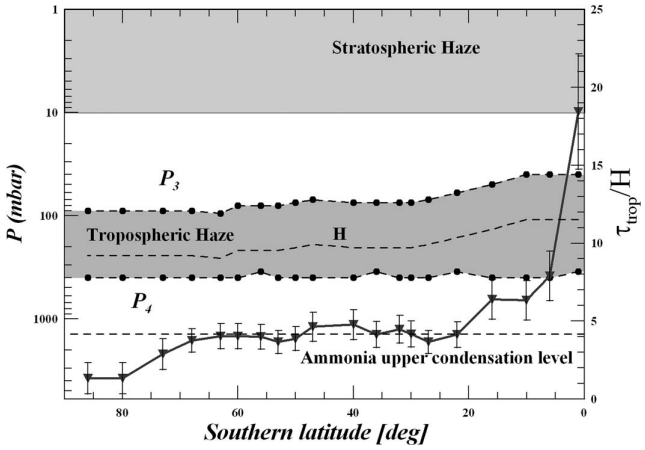

Fig. 12. Schematic plot of the Southern Hemisphere cloud vertical structure as a function of latitude for year 2002. The altitude location (shaded areas) of the hazes is shown on the left axis. The great variations in optical thickness, here shown as the optical thickness per scale height H (triangles and continuous line) with the scale given on the right axis, strongly affect Saturn's visual appearance. The dashed line show the pressure level one scale height below the top of the haze layer (left axis). Note the large differences between pole and equator. The ammonia upper condensation level is also shown as a reference for the location of the main cloud deck. Typical errors for P_2 are ±10 mbar for most latitudes and for P_1 about ±100 mbar.

systematic changes in reflectivity over a full Saturn season, using a self-consistent set of observations.

5.1. Stratospheric changes

The optical thickness of the stratospheric layer varied quite substantially over the period of our observations. Fig. 13 shows the temporal evolution for three different filters at three selected latitudes, representative of each of the main regions of Saturn.

There is a clear increase of τ_2 from 1994 to 2003 in the UV filters. We have plotted linear fits to data in order to show this rise. This effect is most apparent at polar latitudes, where the ratio of the estimated optical thickness in 2003 and 1994 is a factor ∼2. This decreases to ∼1.5 at the equator and to ∼1.15 at the mid-latitudes, showing a general increase of the optical thickness with time at UV wavelengths. This general trend agrees with the changes of insolation at the top of the atmosphere, also shown in Fig. 13. The increase is similar at equatorial and mid-latitudes and much sharper at the pole.

The optical thickness at red wavelengths, similar to that of the deep-methane filter at the equator, is always weakly decreasing over the time period of our observations. Whenever the optical thickness is larger at short wavelengths the decrease with time at red wavelengths is much stronger.

Close to the ring-crossing epoch, we occasionally detect short-duration, strong variations in some filters. There is sometimes a local maximum in haze optical thickness in 1996 or 1997 with a strong decrease after that point and a "normal" behavior after that. This effect has been detected up to 40° S, suggesting that it might be related to the ring-shadowing effect.

But the nature of stratospheric particles shows no change at all. There is no variation in their optical properties and this suggests that the processes that lead to their formation do not vary with time and depend more strongly on location over the planet. That is, polar particles may increase in abundance, but they do not transform into the kind of particles that are found in the mid-latitudes.

5.2. Tropospheric changes

From our study, we find that most of the changes take place in the tropopause region. Among the mid-term, dy-

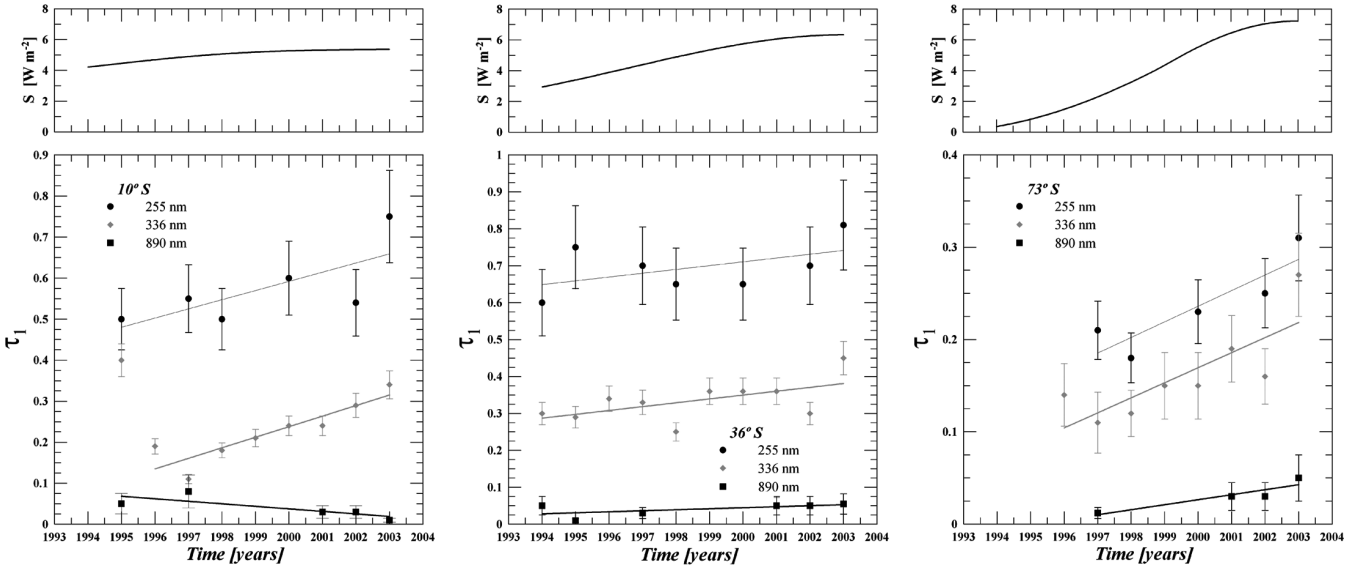

Fig. 13. Temporal variation of the optical thickness of the stratospheric haze at three wavelengths and three latitudes (bottom panels). There is a general increase at short wavelengths (shown with linear fits), which are most sensitive to this parameter. The variation of the average diurnal insolation S at the selected latitudes with time is also shown (upper panels).

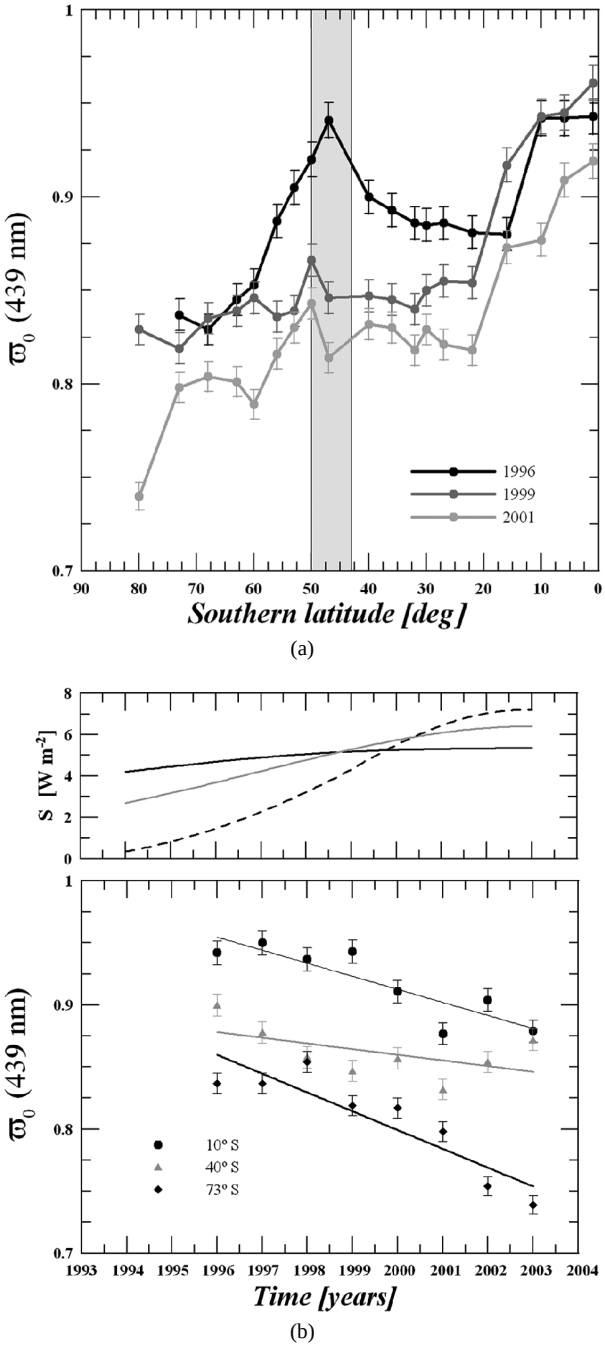

Fig. 14. Comparison between different time-scales variations in the same parameter: (a) Modelling indicates that changes in the single scattering albedo are primarily responsible for the progressive darkening of the region around 47° S shown in Fig. 4. (b) Progressive darkening of the tropospheric particles with time at three latitudes. Linear fits for each latitude are also shown. This general effect is superimposed on local changes and is not homogeneous in the whole hemisphere.

namically generated changes of reflectivity, we can distinguish three different types:

(1) individual features (whose tropospheric structure can be reproduced by our model as shown in Sánchez-Lavega et al., 2004);
(2) reflectivity variations of relatively narrow latitude bands in time-scales of months; and
(3) longer-duration changes, similar to (2) but with time-scales of years.

All of these are sometimes subtle in absolute reflectivity but always strong in visual contrast.

Fig. 14 shows a good comparison between two different time-scales variations acting on the same parameter at the same wavelength. The single scattering albedo $\bar{\omega}_0$ is a very sensitive parameter of the model, showing high variability, probably due to changes in the optical properties of the particles or in the particle size. Fig. 14a shows how the local variation of the reflectivity at about 47° S shown in Fig. 4 is well modelled as a variation of the single scattering albedo. An example of the long-term evolution of the tropospheric haze is the progressive darkening of the particles, most noticeable at 439 nm, but also visible at other wavelengths. These changes follow the insolation variation shown in the upper panel of Fig. 14b.

We found no obvious difference in the pressures between which the tropospheric haze is located. The top level varies, but always within a small deviation around the mean value. The deviations found are almost always below ±10 mbar. This suggests that there is a latitude-dependent mechanism that fixes the pressure level of the top of the tropospheric haze layer, such as the vertical stability of the atmosphere.

The most temporally variable parameter is the optical thickness of the tropospheric haze. It is the key parameter in explaining the atmospheric changes between 1994 and 2003, as long as most of the dynamics we see are taking place in the troposphere. The variations of this parameter are evident, as shown in Fig. 15, and are much larger than the modelling errors.

Fig. 15 shows the extremely strong variation of the optical thickness of the tropospheric haze with time for some latitudes. We have divided the Southern Hemisphere into four regions, one for the Equatorial Zone (Fig. 15a), two for the mid-latitudes (Figs. 15b and 15c) and the last one for the polar region (Fig. 15d). The changes at the equator are about a factor ∼4, whereas for the rest of latitudes, it is about a factor ∼2.

The optical thickness changes follow a similar pattern for all latitudes: τ_1 increases after the ring-crossing epoch and then reduces again reaching a value that seems to be stable. There is some tendency for the maximum of optical thickness to be reached later at more southern latitudes, at least at non-equatorial latitudes. At middle and polar latitudes the optical thickness reached its maximum in the 1995–1999 period. The equator follows a slightly different pattern, because there is a secondary maximum in the 2000–2002 period that is not so clear at other latitudes. Strongly peaked behavior at the equatorial latitudes is not new (Ortiz et al., 1996) and may be better explained, because of its link with observed atmospheric activity (Sánchez-Lavega et al., 1999), similarly to Acarreta and Sánchez-Lavega (1999), by the ascent of the

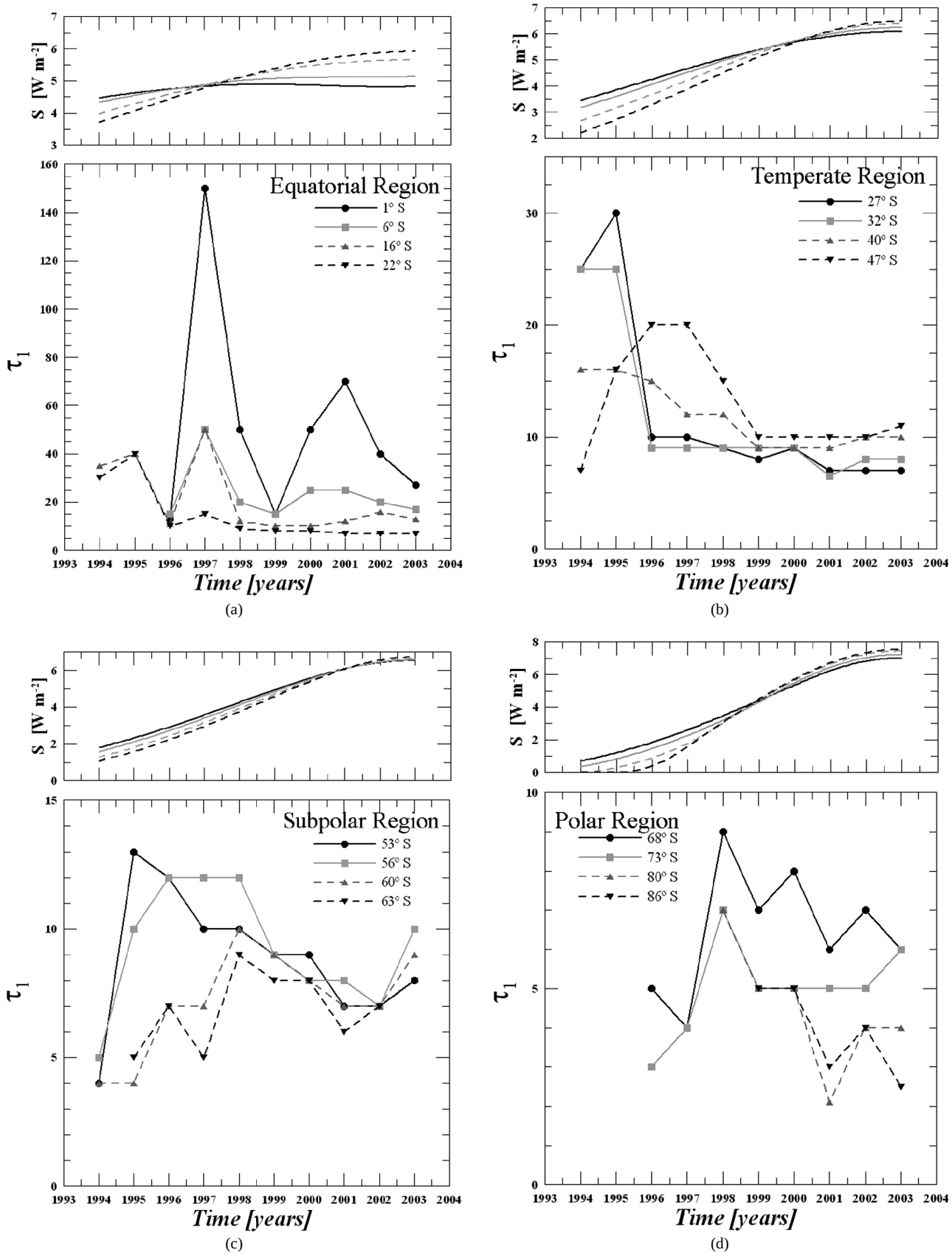

Fig. 15. Temporal variations of the tropospheric optical thickness at selected latitudes from the equator to the pole and the corresponding variation of insolation with time. In (a) the Equatorial Zone is shown; the mid-latitudes are divided between (b) and (c). (d) Panel is for the polar region. The activity at low latitudes is pronounced in 1997, but also seems to be increasing in 2001. Typical errors are ∼20%, but the minimum absolute uncertainty is about ±2.

bottom ammonia cloud, allowing lower values of the optical thickness of the haze.

In Fig. 15 we also show the dependence of insolation S at the top of the atmosphere at the selected latitudes. The maximum insolation is reached at the southern summer solstice epoch and it almost always coincides with a minimum in the optical thickness of the tropospheric haze. It should be noted, however, that the atmosphere is not expected to adjust its temperature instantaneously to the insolation changes, but accordingly with its characteristic response time. As explained, for example, in Barnet (1990), the radiative time constant for Saturn between 1 and 100 mbar is ∼12 years and typically ∼20 years at 400 mbar.

In summary, we have clearly detected strong temporal changes in the tropospheric haze and isolated different contributions. The optical thickness decreases at almost all latitudes, as the insolation increases, but changes are abrupt, in general. However, the pressure levels bounding the tropospheric haze do not change substantially. Superimposed to this evolution of the haze, there are other localized changes, such as the albedo change at about 47° S.

6. Discussion and conclusions

Our study allows us to draw some robust conclusions about the vertical structure of Saturn's upper clouds at the Southern Hemisphere over the period between 1994 and 2003. In this section, we will review and compare them with previous studies.

6.1. Haze mean properties

The upper, stratospheric haze is located at high levels and assumed to extend down to a pressure of ∼10 mbar. The stratospheric particles are small (radii ∼0.2 μm) and, assuming they are Mie scatterers, their refractive indices are $m_r \sim 1.5$ and $m_i \sim 0.1$–0.001. Thus, the optical thickness of this upper haze is strongly dependent on wavelength, varying from ∼0.5 at 255 nm to ∼0.05 at 890 nm.

Previous studies modelled the stratospheric haze in various ways. Karkoschka and Tomasko (1993) extended the haze down to the tropopause, whereas Ortiz et al. (1996) obtained a haze located between ∼20 and ∼50 mbar. Muñoz et al. (2004) followed Stam et al. (2001) and their levels are very similar to ours. The existence of an aerosol-free layer between the stratospheric and the tropospheric haze was proposed to explain Pioneer 11 polarization measurements (Tomasko et al., 1984), so models including such a gap between hazes are favored. Optical thicknesses are also in the same range as in Stam et al. (2001) or Muñoz et al. (2004). Substantial differences are found, however, in the other properties of the stratospheric particles, given that most of previous authors (e.g., Ortiz et al. (1996) or Muñoz et al. (2004)) used a somewhat lower real refractive index (∼1.43) and smaller particles. However, our imaginary refractive indexes coincide with those of Karkoschka and Tomasko (1993).

A second haze layer exists close to the tropopause. We model the bottom pressure of this layer to be at ∼400 mbar. The optical thickness of the tropospheric haze shows very weak wavelength dependence. This dependency could be due either to particle size or to vertical distribution.

The tropospheric haze is represented by a double Henyey–Greenstein function similar to that given by Tomasko and Doose (1984). The single scattering albedo varies strongly with wavelength. Particles are absorbent at shorter wavelengths ($\bar{\omega}_0 \sim 0.7$ or even less at 336 nm) and are almost perfect scatterers at near-IR ($\bar{\omega}_0 \sim 1.0$).

Agreement in obtained results for the tropospheric haze, despite of the differences with previous works in many assumptions about it, is remarkable. Karkoschka and Tomasko (1993) obtained a single scattering albedo of their tropospheric particles very similar to our fitted results. The levels we obtain for the top and the bottom of the tropospheric haze are almost identical to those by Stam et al. (2001) and there is a general agreement in the approximate pressure levels with previous work. Optical thicknesses also agree reasonably well. Karkoschka and Tomasko (1993) estimated $\tau \sim 10$ at mid-northern latitudes and Ortiz et al. (1996) gave values of $\tau/\Delta z$ similar to those presented in Fig. 12. Values by Muñoz et al. (2004) show the greatest differences, about a 20% from ours, but these are within estimated error bars. Based on a completely different spectral range, Stam et al. (2001) estimated values of the optical thickness at visual wavelengths within our expected results.

We include in our a model a semi-infinite cloud at the ammonia condensation level (∼1.4 bar), putatively formed by ammonia ice, but the broadband reflectivity of the planet from the UV to near-IR is not strongly affected by this cloud layer, and our results are not dependent on the detailed nature of the ammonia cloud deck.

6.2. Latitudinal variability

There are important latitudinal differences in both Saturn's upper hazes. The stratospheric particles are slightly smaller at low latitudes, but the strongest change in this layer is found at the pole. The polar particles are darker at the UV and smaller than at any other location. Similar results were also found by Karkoschka and Tomasko (1993) in the Northern Hemisphere, where they located the region of change at about 70° N. Muñoz et al. (2004) stated that the layered model broke down at 60° S; in contrast, we find some of our best fits at this high latitude without substantially changing our vertical model.

However, the most important latitudinal variations are located in the tropospheric haze. The haze is higher and thicker at the equator, changing its top pressure from ∼40 to ∼100 mbar, in the polar region. Particles also change their single scattering albedo locally, with a general tendency to darker particles in higher latitudes.

This latitudinal behavior of the tropospheric haze is well known. Karkoschka and Tomasko (1993) located the top level at levels decreasing with latitude. They also correlated the optical thickness with the zonal wind profile, but we have not detected such correlation at our modelling spatial resolution. In agreement with Stam et al. (2001), whose limiting levels agree with ours, and Muñoz et al. (2004), apart from the polar latitudes discussed above, we also find higher and thicker tropospheric haze in the equatorial latitudes.

6.3. Temporal changes

The most intriguing changes are the temporal ones. From 1994 to 2003 the optical thickness of the tropospheric haze varied strongly, whereas other parameters such as the stratospheric haze's optical thickness or the single scattering albedo of the tropospheric particles show only little variation. The top level of the tropospheric haze suffered almost no variation from one year to another.

Some trends are clear in our results. As shown in Fig. 13, the optical thickness of the stratospheric haze varies linearly with time. This could be related to a rapid response to the continuous change of insolation, given that the polar stratospheric haze suffers the strongest change. If this is correct, it means that the stratospheric optical thickness is controlled by sunlight pointing clearly to a photochemical origin. The same happens with the single scattering albedo of the tropospheric particles, which is inversely related to insolation changes, although there are important local and latitudinal variations. For example, at $\sim 50^\circ$ S, we have detected the progressive brightening and darkening of a complete band. Such tropospheric changes are quite common, sometimes occurring over a time period as short as a few months. In view of the rapidity of these changes, they are probably of dynamical origin, rather than associated with longer-term insolation changes. We will address these issues in a future work.

The variations in the optical thickness of the tropospheric haze also follow a clear pattern at non-equatorial latitudes. Whereas at the equator we find important deviations from a general trend, the troposheric haze at the mid-latitudes clearly shows the winter to summer evolution. It does not change its top level but its optical thickness, leading to a brighter atmosphere at short and darker at long wavelengths. For the first time, the evolution from a "hazy" to a "clear" troposphere detected from a ring plane crossing epoch to the next has been followed and analyzed in terms of a radiative transfer model. However, the variations seem to be too abrupt to be generated only by a change in the insolation, and it is likely that dynamical effects are needed to explain such strong increases.

This temporal behavior of the tropospheric haze was anticipated in previous studies, such as West (1982), Sánchez-Lavega et al. (1993) or Stam et al. (2001). Other studies have dealt with the hemispheric asymmetries in order to analyze this same phenomenon, mainly Muñoz et al. (2004). This hemispheric asymmetry was also found in the Voyager IRIS far-infrared measurements (Conrath and Pirraglia, 1983), with the Northern (summer) Hemisphere colder than the Southern. Bézard et al. (1984) modelled this phenomenon and found strong insolation changes to be responsible of such asymmetry.

In fact, solar heat deposition models could now be improved. Previous models have been limited by uncertainties in the properties of Saturn's atmospheric aerosols (Barnet et al., 1992a). Our new results on the spatial distribution and temporal evolution of clouds and hazes in Saturn's atmosphere allow a more detailed analysis of the influence of haze particles on the atmospheric dynamics of the planet. Linking radiative and dynamical phenomena, such as exploring the heating rates at different atmospheric levels, would be a logical next step. This would have a direct application on the physics of thermal-waves present at the upper troposphere and lower stratosphere detected in the Voyager IRIS data (Achterberg and Flasar, 1996).

Cassini observations to be made in the coming years will complement our Hubble Space Telescope observations, studying the atmosphere from the southern summer to the southern fall, and finally leading to the next ring plane crossing, when an inverse hemispheric asymmetry is expected. But much can be done with the data set we have presented. First, the hemispheric asymmetry in 1995 and adjacent years can be analyzed in detail by modelling the northern latitudes and comparing the results with the southern ones. Second, once we have fixed a mean model that accurately reproduces the observations, mid-term changes, in two or three months period, can be explained in terms of a vertical model, addressing the rapid atmospheric changes not covered by this work. All of this observational and modelling effort will result in a better understanding of Saturn's atmosphere and, as an extension, of the giant planets.

Acknowledgments

S.P.-H., A.S.-L., and J.F.R. were supported by the MCYT Plan Nacional de Astronomía y Astrofísica 2003-03216, Grupos UPV 13697/2001 and Fondos FEDER. S.P.-H. acknowledges a PhD fellowship from the Spanish MEC. R.G.F. was supported in part by NASA's Planetary Geology and Geophysics Program NAG5-10197 and an STSCI Grant GO-08660.01A. The NASA/ESA Hubble Space Telescope is operated by the Association of Universities for Research in Astronomy under NASA Contract NAS5-26555. We thank J.A. Cano (GEA, Spain) for the use of the software LAIA and J.R. Acarreta for the development of the radiative transfer codes and many helpful comments and suggestions.

References

Acarreta, J.R., Sánchez-Lavega, A., 1999. Vertical cloud structure in Saturn's 1990 Equatorial Storm. Icarus 137, 24–33.

Achterberg, R.K., Flasar, F.M., 1996. Planetary-scale thermal waves in Saturn's upper troposphere. Icarus 119, 350–369.
Barnet C.D., 1990. Saturn's seasonal winds and temperature: the effect of the ring system on the troposphere and stratosphere. Thesis, New Mexico State University.
Barnet, C.D., Beebe, R.F., Conrath, B.J., 1992a. A seasonal radiative-dynamic model of Saturn's troposphere. Icarus 98, 94–107.
Barnet, C.D., Westphal, J.A., Beebe, R.F., Huber, L.F., 1992b. Hubble Space Telescope observations of the 1990 equatorial disturbance on Saturn—zonal winds and central meridian albedos. Icarus 100, 499–511.
Bézard, B., Gautier, D., Conrath, B., 1984. A seasonal model of the saturnian upper troposphere: comparison with Voyager infrared measurements. Icarus 60, 274–288.
Briggs, F.H., Sackett, P.D., 1989. Radio observations of Saturn as a probe of its atmosphere and cloud structure. Icarus 80, 77–103.
Conrath, B.J., Pirraglia, J.A., 1983. Thermal structure of Saturn from Voyager infrared measurements: implications for atmospheric dynamics. Icarus 53, 286–292.
Cuzzi, J.N., French, R.G., Dones, L., 2002. HST multicolour (255–1042 nm) photometry of Saturn's main rings. I. Radial profiles, phase and opening angle variations, and regional spectra. Icarus 158, 199–223.
Danielson, R.E., Tomasko, M.G., 1969. A two-layer model of the jovian clouds. J. Atmos. Sci. 26, 889–897.
Dones, L., Cuzzi, J.N., Showalter, M.R., 1993. Voyager photometry of Saturn's A ring. Icarus 105, 184–215.
French, R.G., McGhee, C.A., Dones, L., Lissauer, J.J., 2003. Saturn's wayward shepherds: the peregrination of Prometheus and Pandora. Icarus 162, 143–170.
García-Melendo, E., Sánchez-Lavega, A., 2001. A study of the stability of jovian zonal winds from HST images: 1995–2000. Icarus 152, 316–330.
Grossman, A.W., Muhleman, D.O., Berge, G.L., 1989. High-resolution microwave images of Saturn. Science 245, 1211–1215.
Hansen, J.E., Travis, L.D., 1974. Light scattering in planetary atmospheres. Space Sci. Rev. 16, 527–610.
Henyey, L.C., Greenstein, J.L., 1941. Diffuse radiation in the Galaxy. Astrophys. J. 93, 70–83.
Hueso, R., Sánchez-Lavega, A., 2004. A three-dimensional model of moist convection for the giant planets II: Saturn's water and ammonia moist convective storms. Icarus 172, 255–271.
Irvine, W.M., 1965. Multiple scattering by large particles. Astrophys. J. 142, 1563–1567.
Karkoschka, E., 1998a. WFPC2 Photometry for the Solar System. Space Telescope Science Institute, Baltimore, MD.
Karkoschka, E., 1998b. Methane, ammonia and temperature measurements of the jovian planets and Titan from CCD-spectrophotometry. Icarus 133, 134–146.
Karkoschka, E., Tomasko, M.G., 1992. Saturn's upper troposphere 1986–1989. Icarus 97, 161–181.
Karkoschka, E., Tomasko, M.G., 1993. Saturn's upper atmospheric hazes observed by the Hubble Space Telescope. Icarus 106, 428–441.
Lindal, G.F., Sweetnam, D.N., Eshleman, V.R., 1985. The atmosphere of Saturn—an analysis of the Voyager radio occultation measurements. Astron. J. 90, 1136–1146.
Liou, K.N., 1992. Radiation and Cloud Processes in the Atmosphere. Oxford Univ. Press, New York.
Macy, W., 1977. Inhomogeneous models of the atmosphere of Saturn. Icarus 32, 328–347.
Martonchik, J.V., Orton, G.S., Appleby, J.F., 1984. Optical properties of NH3 ice from the far infrared to the near ultraviolet. Appl. Optics 23, 541–547.
Muñoz, O., Moreno, F., Molina, A., Grodent, D., Gérard, J.C., Dols, V., 2004. Study of the vertical structure of Saturn's atmosphere using HST/WFPC2 images. Icarus 169, 413–428.
Ortiz, J.L., Moreno, F., Molina, A., 1996. Saturn 1991–1993: clouds and hazes. Icarus 119, 53–66.
Poulet, F., Karkoschka, E., Sicardy, B., 1999. Spectrophotometry of Saturn's small satellites and rings from Hubble Space Telescope images. J. Geophys. Res. 104 (E10), 24095–24110.
Ramanathan, V., Crutzen, P.J., Kiehl, J.T., Rossenfeld, D., 2001. Aerosols, climate and the hydrological cycle. Nature 294, 2119–2124.
Sánchez-Lavega, A., Battaner, E., 1986. Long-term changes in Saturn's atmospheric belts and zones. Astron. Astrophys. Suppl. Ser. 64, 287–301.
Sánchez-Lavega, A., Colas, F., Lecacheux, J., Laques, P., Miyazaki, I., Parker, D., 1991. The Great White Spot and disturbances in Saturn's Equatorial atmosphere during 1990. Nature 353, 397–401.
Sánchez-Lavega, A., Colas, F., Lecacheux, J., Laques, P., 1993. Temporal behavior of cloud morphologies and motions in Saturn's atmosphere. J. Geophys. Res. 98, 18857–18872.
Sánchez-Lavega, A., Lecacheux, J., Gomez, J.M., Colas, F., Laques, P., Noll, K., Gilmore, D., Miyazaki, I., Parker, D., 1996. Large-scale storms in Saturn's atmosphere during 1994. Science 271, 631–634.
Sánchez-Lavega, A., Lecacheux, J., Gomez, J.M., Colas, F., Rojas, J.F., Gómez, J.M., 1999. Discrete cloud activity in Saturn's equator during 1995, 1996 and 1997. Planet. Space Sci. 47, 1277–1283.
Sánchez-Lavega, A., Rojas, J.F., Sada, P.V., 2000. Saturn's zonal winds at cloud level. Icarus 147, 405–420.
Sánchez-Lavega, A., Pérez-Hoyos, S., Acarreta, J.R., French, R.G., 2002. No hexagonal wave around Saturn's Southern Pole. Icarus 160, 216–219.
Sánchez-Lavega, A., Pérez-Hoyos, S., Hueso, R., Rojas, J.F., French, R.G., 2003. A strong decrease in Saturn's Equatorial jet at cloud level. Nature 423, 623–625.
Sánchez-Lavega, A., Hueso, R., Pérez-Hoyos, S., Rojas, J.F., French, R.G., 2004. Saturn's cloud morphology and zonal winds before the Cassini encounter. Icarus 170, 519–523.
Stam, D., Banfield, D., Gierasch, P.J., Nicholson, P.D., 2001. Near-IR spectrophotometry of Saturnian aerosols—meridional and vertical distribution. Icarus 152, 407–422.
Tomasko, M.G., Doose, L.R., 1984. Polarimetry and photometry of Saturn from Pioneer 11: observations and constraints on the distribution and properties of cloud and aerosol particles. Icarus 58, 1–34.
Tomasko, M.G., West, R.A., Orton, G.S., Tejfel, V.G., 1984. Cloud and aerosols in Saturn's atmosphere. In: Gehrels, T., Matthews, M.S. (Eds.), Saturn. Univ. of Arizona Press, Tucson, AZ, pp. 150–194.
van de Hulst, H.C., 1981. Light Scattering by Small Particles. Dover, New York.
Weidenschilling, S.J., Lewis, J.S., 1973. Atmospheric and cloud structures of the jovian planets. Icarus 20, 465–476.
West, R.A., 1982. Spatially resolved methane band photometry of Saturn: I. Absolute reflectivity and center-to-limb variations in the 6190-, 7250-, and 8900-A bands. Icarus 51, 51–64.
West, R.A., 1983. Spatially resolved methane band photometry of Saturn: II. Cloud structure models at four latitudes. Icarus 53, 301–309.
West, R.A., Sato, M., Hart, H., Lane, A.L., Hord, C.W., Simmons, K.E., Esposito, L.W., Coffeen, D.L., Pomphrey, R.B., 1983. Photometry and polarimetry of Saturn at 2640 and 7500 A. J. Geophys. Res. 88, 8679–8697.
Young, R.E., 2003. The Galileo probe: how it has changed our understanding of Jupiter. New Astron. Rev. 47, 1–51.